

1 Pathogenic mutations in the chromokinesin KIF22 disrupt anaphase chromosome 2 segregation

3
4 Alex F. Thompson¹, Patrick R. Blackburn^{2,3}, Dusica Babovic-Vuksanovic^{2,4}, Jane B. Lian⁵, Eric
5 W. Klee⁶, Jason K. Stumpff^{1*}

6
7 ¹Molecular Physiology and Biophysics, University of Vermont, Burlington, VT

8 ²Laboratory Medicine and Pathology, Mayo Clinic, Rochester, MN

9 ³Pathology, St. Jude Children's Research Hospital, Memphis, TN

10 ⁴Clinical Genomics, Mayo Clinic, Rochester, MN

11 ⁵Biochemistry, University of Vermont, Burlington, VT

12 ⁶Biomedical Informatics, Mayo Clinic, Rochester, MN

13 *Corresponding author, jason.stumpff@uvm.edu

14

15 **Running Title:** KIF22 mutations disrupt chromosome segregation

16

17

18 **ABSTRACT**

19 The chromokinesin KIF22 generates pushing forces that contribute to mitotic chromosome
20 congression and alignment. Mutations in the motor domain of KIF22 have been identified in
21 patients with abnormal skeletal development, and we report the identification of a patient with a
22 novel mutation in the KIF22 tail. We assessed whether pathogenic mutations affect the function
23 of KIF22 in mitosis and demonstrate that mutations do not result in a loss of KIF22 function.
24 Instead, mutations disrupted chromosome segregation in anaphase, resulting in reduced
25 proliferation, abnormal daughter cell nuclear morphology and, in a subset of cells, cytokinesis
26 failure. This phenotype could be explained by a failure of KIF22 to inactivate in anaphase.
27 Consistent with this model, constitutive activation of the motor phenocopied the effects of
28 pathogenic mutations. These findings offer insight into the mechanism by which mutations in
29 KIF22 may affect human development, the consequences of imbalance between polar ejection
30 forces and antiparallel microtubule sliding in anaphase, and potential mechanisms of KIF22
31 regulation.

32

33 **INTRODUCTION**

34 Mitosis requires mechanisms that mechanically control chromosome movements to
35 ensure equal segregation of chromosomes to daughter cells. Forces that move mitotic
36 chromosomes are generated by microtubule dynamics within the mitotic spindle and by molecular
37 motor proteins. The chromokinesin KIF22 (or Kid, kinesin-like DNA-binding protein) is a plus-end
38 directed member of the kinesin-10 family (Yajima et al. 2003). KIF22 and its orthologs, including
39 Nod (*Drosophila melanogaster*) (Zhang et al. 1990) and Xkid (*Xenopus laevis*) (Funabiki and

40 Murray 2000; Takagi et al. 2013; Antonio et al. 2000), generate forces that move chromosomes
41 away from the spindle poles. Structurally, KIF22 contains a conserved kinesin motor domain
42 responsible for ATP hydrolysis and microtubule binding (Tokai et al. 1996; Yajima et al. 2003), a
43 second microtubule binding domain in the tail (Shiroguchi et al. 2003), a predicted coiled-coil
44 domain (Shiroguchi et al. 2003), and a C-terminal DNA binding domain which includes a helix-
45 hairpin-helix motif (Tokai et al. 1996) (**Figure 1A**).

46 In interphase, KIF22 localizes to the nucleus (Tokai et al. 1996; Levesque and Compton
47 2001). As cells enter mitosis, chromosomes condense and KIF22 binds along chromosome arms
48 (Tokai et al. 1996; Levesque and Compton 2001). In prometaphase, chromosomes must
49 congress and align at the center of the spindle. The interactions of the KIF22 motor domain with
50 spindle microtubules and the KIF22 tail domain with chromosome arms allows the motor to
51 generate polar ejection forces (Brouhard and Hunt 2005; Bieling et al. 2010), which push the arms
52 of chromosomes away from the spindle poles and towards the center of the spindle (Rieder et al.
53 1986; Rieder and Salmon 1994; Marshall et al. 2001), contributing to chromosome congression
54 in prometaphase (Levesque and Compton 2001; Wandke et al. 2012; Iemura and Tanaka 2015),
55 as well as chromosome arm orientation (Levesque and Compton 2001; Wandke et al. 2012). In
56 metaphase, polar ejection forces also contribute to chromosome oscillation and alignment
57 (Funabiki and Murray 2000; Antonio et al. 2000; Levesque and Compton 2001; Levesque et al.
58 2003; Tokai-Nishizumi et al. 2005; Stumpff et al. 2012; Takagi et al. 2013). Purified KIF22 is
59 monomeric (Shiroguchi et al. 2003), and the forces generated by KIF22 on chromosome arms
60 may represent the collective action of many monomers. In anaphase, KIF22 is inactivated to
61 reduce polar ejection forces and allow chromosomes to segregate towards the spindle poles
62 (Soeda et al. 2016; Su et al. 2016; Wolf et al. 2006)

63 The generation of polar ejection forces by KIF22 is regulated by the activity of cyclin-
64 dependent kinase 1 (CDK1)/cyclin B, which is high in prometa- and metaphase, and drops sharply
65 at the metaphase to anaphase transition when cyclin B is degraded (Morgan 1995; Hershko
66 1999). KIF22 is phosphorylated by CDK1/cyclin B at T463, a residue in the tail of the motor
67 between the second microtubule binding and coiled-coil domains. Phosphorylation of T463 is
68 required for polar ejection force generation in prometa- and metaphase, and dephosphorylation
69 of T463 is necessary for the suspension of polar ejection forces to allow chromosome segregation
70 in anaphase (Soeda et al. 2016). Reduced polar ejection forces in anaphase are one component
71 of an overall shift in force balance at the metaphase to anaphase transition as microtubule
72 dynamics and motor activities change to promote anaphase chromosome segregation rather than
73 metaphase congression. In addition to its activity, the expression level of KIF22 is also regulated

74 as the cell cycle progresses. Expression is highest in G2 phase and mitosis, and drops as cells
75 exit mitosis (Germani et al. 2000; Yount et al. 2015).

76 Mutations in KIF22 have been identified in patients with a developmental disorder,
77 spondyloepimetaphyseal dysplasia with joint laxity, leptodactylic type (SEMDJL2, also referred to
78 as Hall Type or lepto-SEMDJL) (Min et al. 2011; Boyden et al. 2011; Tüysüz et al. 2014). Four
79 point mutations in two amino acids have been reported in SEMDJL2 patients (Min et al. 2011;
80 Boyden et al. 2011; Tüysüz et al. 2014) (**Figure 1A**). These mutations occur in adjacent residues
81 P148 and R149 in the $\alpha 2$ helix of the KIF22 motor domain (**Figure 1B**). P148 and R149 are
82 conserved in kinesin-10 family members across species (**Figure 1C**) and in many human
83 members of the kinesin superfamily (**Figure 1D**). However, no pathogenic mutations in the
84 homologous proline or arginine residues have been recorded in OMIM (Online Mendelian
85 Inheritance in Man, <https://omim.org/>). All identified patients are heterozygous for a single
86 mutation in KIF22. Mutations dominantly cause SEMDJL2, and patients with both *de novo* and
87 inherited mutations in KIF22 have been identified (Min et al. 2011; Boyden et al. 2011).

88 Although KIF22 mRNA is expressed throughout the body (Human Protein Atlas,
89 <http://www.proteinatlas.org> (Uhlen et al. 2015)), the effects of these mutations are largely tissue-
90 specific, and the development of the skeletal system is most affected in SEMDJL2 patients. A
91 primary symptom of SEMDJL2 is short stature, resulting from shortening of both the trunk and the
92 limbs. Additionally, patients present with joint laxity, midface hypoplasia, scoliosis, and
93 leptodactyly, a narrowing of the fingers (Min et al. 2011; Boyden et al. 2011). In very young
94 children, the softness of the cartilage in the larynx and trachea can cause respiratory issues
95 (Boyden et al. 2011). Growth plate radiology demonstrated delayed maturation of the metaphyses
96 and epiphyses in SEMDJL2 patients, and symptoms became more pronounced as patients aged
97 (Tüysüz et al. 2014). Leptodactyly, specifically, was only observed in older (young adult) patients
98 (Boyden et al. 2011).

99 Pathogenic mutations in the KIF22 motor domain were predicted to be loss of function
100 mutations (Min et al. 2011). However, KIF22 knockout in mice did not affect skeletal development.
101 Loss of KIF22 was lethal early in embryogenesis for approximately 50% of embryos, but mice that
102 survived past this point developed to adulthood and demonstrated no gross abnormalities or
103 pathologies (Ohsugi et al. 2003). As such, the cellular mechanism by which mutations in KIF22
104 affect development is unknown.

105 Here we characterize an additional patient with a mutation in KIF22 and assess the effect
106 of previously reported and novel pathogenic mutations on the function of KIF22 in mitosis. We
107 demonstrate that mutations are not loss of function mutations, and do not alter the localization of

108 the motor or the generation of polar ejection forces in prometaphase. Instead, mutations disrupt
109 anaphase chromosome segregation, consistent with continued KIF22 activation and consequent
110 polar ejection force generation in anaphase. Defects in anaphase chromosome segregation affect
111 daughter cell nuclear morphology and, in a subset of cells, prevent cytokinesis. These findings
112 demonstrate that anaphase inactivation of KIF22 is critical for daughter cell fitness. As such,
113 mitotic defects may contribute to pathogenesis in patients with KIF22 mutations. Additionally, we
114 demonstrate that aberrant polar ejection force generation in anaphase is sufficient to affect the
115 movements of not only the chromosomes but also the spindle poles, offering insight into the
116 balance of forces required in anaphase for accurate chromosome segregation.

117

118 **RESULTS**

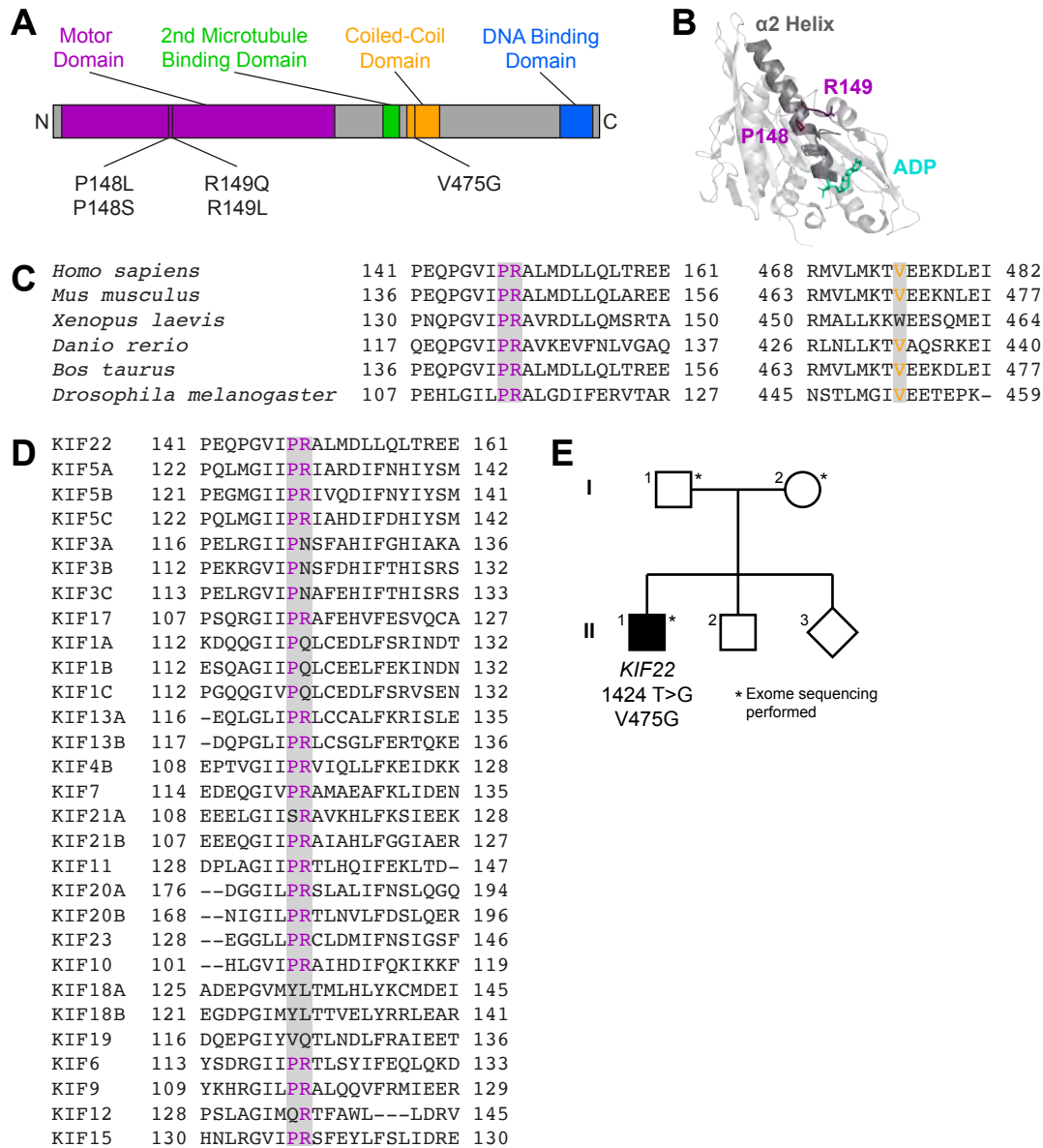
119 **A novel mutation in KIF22 affects development**

120 We report the identification and characterization of a patient with a novel mutation in KIF22
121 (**Figure 1E**). The patient is a 15-year-old male with a history of short stature, cryptorchidism and
122 shawl scrotum, minimal scoliosis, secondary enuresis, and skin hyperpigmentation. He presented
123 for evaluation at 9 years of age. At that time, his height was just below 3% for age, weight was at
124 40% for age, and BMI was 82% for age. He was noted to have relative macrocephaly, with a head
125 circumference at 93% for age. He had a broad forehead and hypertelorism, round face, flaring of
126 eyebrows, and ankyloglossia. He also had mild brachydactyly (**Figure 1F**). He had a history of
127 short stature since infancy, but followed a trajectory close to the third percentile. Growth hormone
128 and thyroid function were normal. Bone age showed a normal, age-appropriate bone maturation
129 with normal epiphyseal ossification centers. However, skeletal survey at age 11 years disclosed
130 mild scoliosis of 14 degrees, as well as mild increase of the central anteroposterior diameter of
131 several lower thoracic vertebrae with mild "bullet-shaped" appearance, mild posterior scalloping
132 of the lumbar vertebrae, and mild foreshortening of both 4th metacarpals (**Figure 1G**).

133 Genetic testing was performed to determine the cause of these developmental
134 differences. Clinical whole exome sequencing revealed two variants of uncertain significance: a
135 maternally inherited heterozygous *SLC26A2* variant [NM_000112.3(*SLC26A2*): c.1046T>A
136 (p.F349Y)] (SCV000782516.1) as well as a *de novo* heterozygous *KIF22* variant
137 [NM_007317.3(*KIF22*):c.1424T>G (p.V475G)] (SCV000782515.1) (**Figure 1E**). The *SLC26A2*
138 gene encodes the diastrophic dysplasia sulfate transporter (Rossi and Superti-Furga 2001; Haila
139 et al. 2001). However, results of carbohydrate deficient transferrin testing were not consistent with
140 a congenital disorder of glycosylation (transferrin tri-sialo/di-oligo ratio 0.07).

141 The c.1424T>G, p.(V475G) *KIF22* variant has not been observed previously in the
142 Genome Aggregation Database (gnomAD). This missense variant has mixed *in silico* predictions
143 of significance. V475G is predicted to be deleterious by Sorting Intolerant from Tolerant (SIFT)
144 (Vaser et al. 2015) (score 0.01 with scores ranging from 0 to 1 and scores below 0.05 considered
145 deleterious), benign by Polymorphism Phenotyping (PolyPhen-2) (Adzhubei et al. 2010) (score
146 0.437), deleterious by MutationTaster (Schwarz et al. 2010), which employs a Bayes classifier to
147 predict the disease potential of a variant, deleterious by Combined Annotation Dependent
148 Depletion (CADD) (Rentzsch et al. 2018) (scaled C-score 15.3800, with a score of greater than
149 or equal to 10 indicating a deleterious substitution), deleterious by Deleterious Annotation of
150 Genetic Variants Using Neural Networks (DANN) (Quang et al. 2015) (score 0.99 with scores
151 ranging from 0 to 1 and higher values indicating a variant is more likely to be deleterious), and
152 benign using Rare Exome Variant Ensemble Learner (REVEL) (Ioannidis et al. 2016) (score 0.28
153 with scores ranging from 0 to 1 and scores >0.803 classified as pathogenic). According to
154 American College of Medical Genetics 2015 criteria, the variant was classified as a variant of
155 uncertain significance (VUS). V475 is located in the coiled-coil domain in the tail of *KIF22* (**Figure**
156 **1A**). This residue is conserved in most kinesin-10 family members across species (**Figure 1C**).
157 However, the tail domains of kinesin motors diverge in both structure and function, and as such
158 meaningful alignments to assess the conservation of V475 across the human kinesin superfamily
159 were not possible.

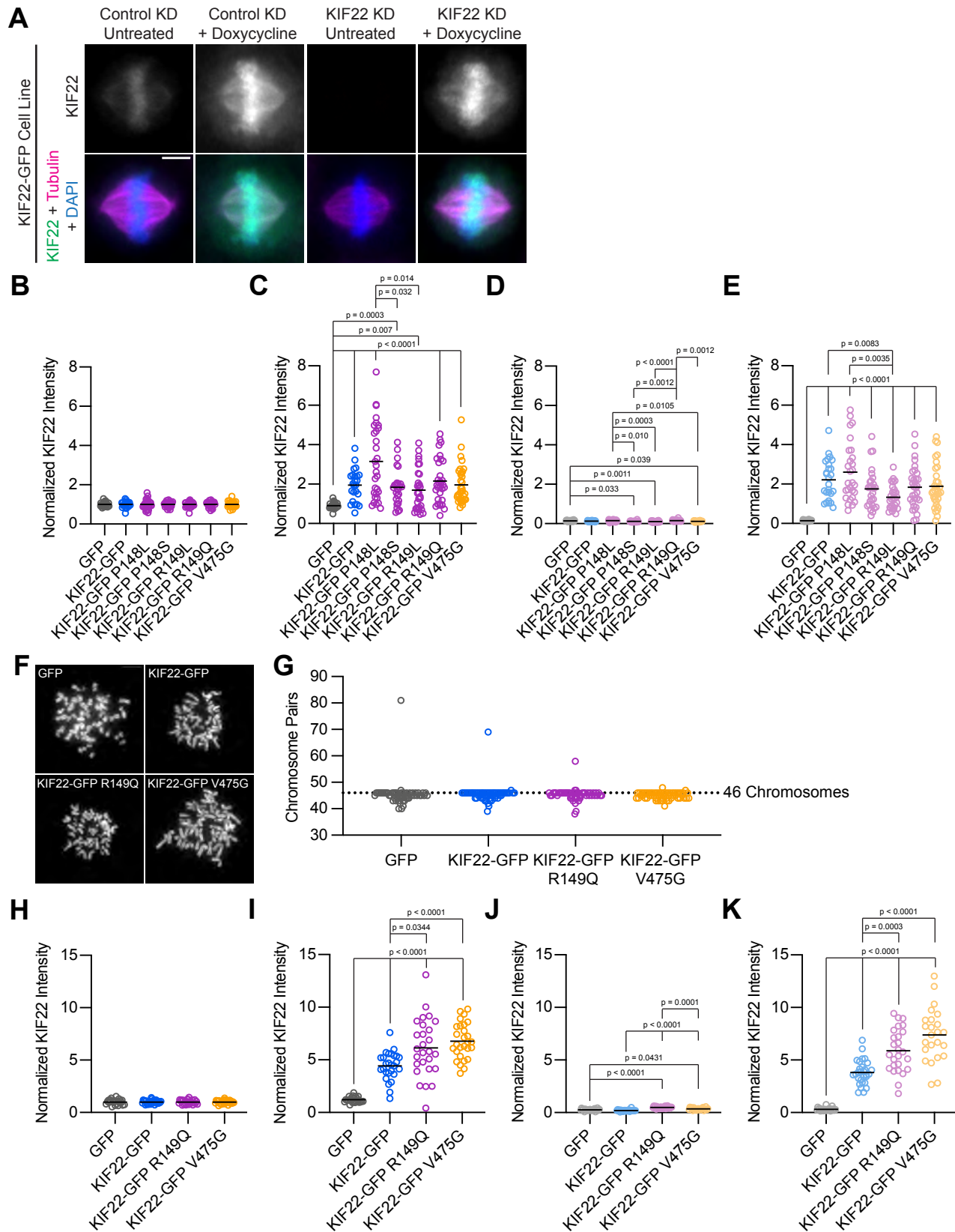
Figure 1



160 **Figure 1. Identification of a novel pathogenic mutation in the tail of KIF22.**

161 **(A)** Schematic of the domains of KIF22 with pathogenic mutations in the motor domain (magenta)
162 and coiled-coil domain (yellow) indicated. **(B)** Location of amino acids P148 and R149 in the
163 alpha-2 helix of the KIF22 motor domain (PDB 6NJE). **(C)** Alignment of amino acid sequences of
164 kinesin-10 family members to assess conservation of motor domain (P148 and R149, left) and
165 coiled-coil domain (V475G, right) residues across species. **(D)** Alignment of amino acid
166 sequences of human kinesin motors to assess conservation of motor domain residues across the
167 kinesin superfamily. For C and D, alignments were performed using Clustal Omega. **(E)** Pedigree
168 identifying the *de novo* V475G (1424 T>G) mutation. **(F)** Radiograph of the patient's hand,
169 posteroanterior view. **(G)** Radiographs of the patient's spine. Left: anteroposterior view of the
170 chest, right: lateral view of the lumbo-sacral spine. Arrowheads indicate "bullet-shaped" vertebrae.

Supplemental Figure 1



171 **Supplemental Figure 1. HeLa-Kyoto and RPE-1 stable cell lines express mutant KIF22.**

172 **(A)** Immunofluorescence images of HeLa-Kyoto cells expressing KIF22-GFP under the control of
173 a doxycycline inducible promoter. Images are maximum intensity projections in z of five frames
174 at the center of the spindle. Fixed approximately 24 hours after siRNA transfection and treatment
175 with doxycycline to induce expression. Scale bar 5 μm . KD: knockdown. **(B-E)** Quantification of
176 KIF22 fluorescence intensity in untreated HeLa-Kyoto cells transfected with control siRNA (B),
177 cells treated with doxycycline to induce expression and transfected with control siRNA (C),
178 untreated cells transfected with KIF22 siRNA (D), and cells treated with doxycycline and
179 transfected with KIF22 siRNA (E) normalized to the mean intensity of uninduced, control
180 knockdown cells (endogenous KIF22 expression level) for each cell line (B). 21-33 HeLa-Kyoto
181 cells per condition from 3 experiments. **(F)** DAPI-stained metaphase chromosome spreads from
182 uninduced RPE-1 cell lines with inducible expression of GFP, KIF22-GFP, KIF22-GFP R149Q, or
183 KIF22-GFP V475G. Scale bar 10 μm . Images are representative of 3 experiments. **(G)** Numbers
184 of chromosome pairs counted in metaphase spreads prepared from RPE-1 stable cell lines.
185 Dashed line indicates the expected chromosome number for diploid human cells (46). The mode
186 for each cell line is 46. 53-58 spreads per condition from 3 experiments. **(H-K)** Quantification of
187 KIF22 fluorescence intensity in untreated RPE-1 cells transfected with control siRNA (H), cells
188 treated with doxycycline to induce expression and transfected with control siRNA (I), untreated
189 cells transfected with KIF22 siRNA (J), and cells treated with doxycycline and transfected with
190 KIF22 siRNA (K) normalized to the mean intensity of uninduced, control knockdown cells for each
191 cell line (H). 21-29 RPE-1 cells per condition from 3 experiments. For B-E and H-K, bars indicate
192 means. p values from Brown-Forsythe and Welch ANOVA with Dunnett's T3 multiple comparisons
193 test. p values are greater than 0.05 for comparisons without a marked p value.

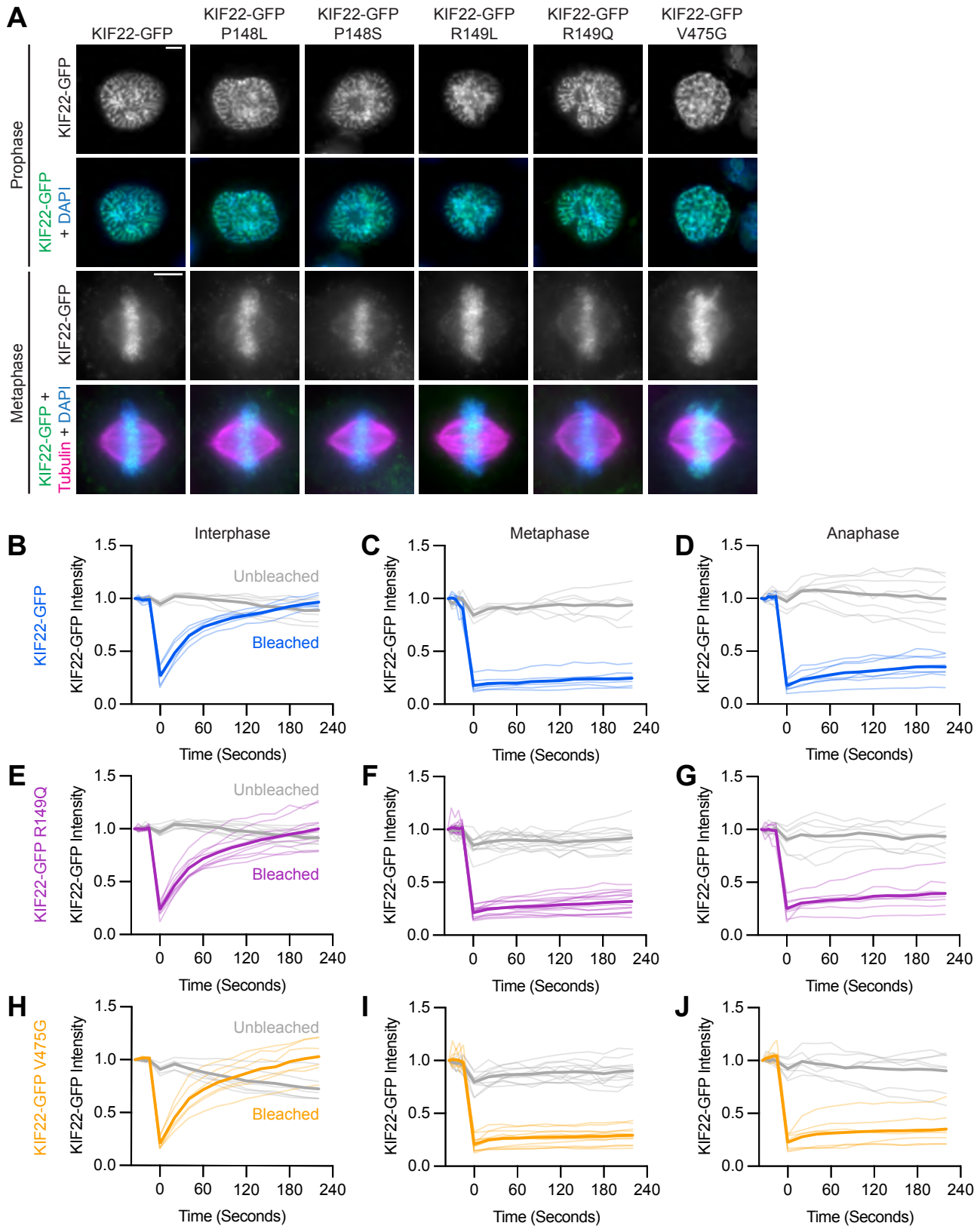
194 **Pathogenic mutations in KIF22 do not disrupt the localization of the motor**

195 To assess the effect of published pathogenic mutations in the motor domain and the novel
196 pathogenic mutation in the tail on the function of KIF22 in mitosis, we generated human cervical
197 adenocarcinoma (HeLa-Kyoto) cell lines with inducible expression of KIF22-GFP. Treatment of
198 these cells with doxycycline induced KIF22-GFP expression at a level approximately two- to three-
199 fold higher than the level of expression of endogenous KIF22 as measured by
200 immunofluorescence (**Figure S1A-C**). To facilitate both overexpression of and rescue with KIF22-
201 GFP constructs, siRNA-resistant silent mutations were introduced into exogenous KIF22 (**Figure**
202 **S1D-E**). siRNA knockdown reduced levels of endogenous KIF22 by 87% (mean knockdown
203 efficiency across HeLa-Kyoto cell lines) (**Figure S1D**). Initial experiments were performed using
204 HeLa-Kyoto cell lines expressing each known pathogenic mutation in KIF22 (P148L, P148S,
205 R149L, R149Q, and V475G), and a subset of experiments then focused on cells expressing one
206 representative motor domain mutation (R149Q) or the coiled-coil domain mutation in the tail
207 (V475G). Additionally, we generated inducible retinal pigmented epithelial (RPE-1) cell lines
208 expressing wild type and mutant KIF22-GFP to assess any differences between the
209 consequences of expressing mutant KIF22 in aneuploid cancer-derived cells (HeLa-Kyoto) and
210 genomically stable somatic cells. RPE-1 cells are human telomerase reverse transcriptase
211 (hTERT)-immortalized (Bodnar et al. 1998), and metaphase chromosome spreads demonstrated
212 that these cell lines are near-diploid, with a modal chromosome number of 46, even after selection
213 to generate stable cell lines (**Figure S1F-G**). The expression level of siRNA-resistant KIF22-GFP
214 in RPE-1 cell lines was approximately four- to seven-fold higher than the level of expression of
215 endogenous KIF22 (**Figure S1H-K**), and siRNA knockdown reduced levels of endogenous KIF22
216 by 67% (mean knockdown efficiency across RPE-1 cell lines measured using
217 immunofluorescence). As measurements of KIF22 depletion by immunofluorescence may include
218 non-specific signal, this estimate of knockdown efficiency may underestimate the depletion of
219 KIF22.

220 KIF22 localizes to the nucleus in interphase, and primarily localizes to chromosomes and
221 spindle microtubules during mitosis (Tokai et al. 1996). KIF22-GFP with pathogenic mutations
222 demonstrated the same localization pattern throughout the cell cycle as wild type motor (**Figure**
223 **2A**). In all cell lines, KIF22-GFP was localized to the nucleus in interphase cells and was bound
224 to condensing chromosomes in prophase. In prometaphase, metaphase, and anaphase mutant
225 and wild type KIF22-GFP localized primarily to chromosome arms, with a smaller amount of motor
226 signal visible on the spindle microtubules. The same localization patterns were seen for mutant
227 and wild type KIF22-GFP expressed in RPE-1 cells (**Figure S2A**).

228 Since mutations did not grossly disrupt localization of KIF22-GFP, fluorescence recovery
229 after photobleaching (FRAP) was used to compare the dynamics of mutant and wild type KIF22
230 localization. In interphase nuclei, KIF22-GFP signal recovered completely 220 seconds after
231 bleaching ($97\% \pm 3\%$ of intensity before bleaching, mean \pm SEM), indicating a dynamic pool of
232 KIF22-GFP (**Figure 2B and S2B**). Similar high recovery percentages were also measured in
233 interphase nuclei of cells expressing KIF22-GFP R149Q and KIF22-GFP V475G ($100\% \pm 6\%$ and
234 $103\% \pm 7\%$ at 220 seconds, respectively) (**Figure 2E and 2H**). In contrast, KIF22-GFP recovery
235 was minimal in cells bleached during metaphase and anaphase. In metaphase cells, immediately
236 after bleaching KIF22-GFP intensity was reduced to $18 \pm 3\%$ of initial intensity, and intensity had
237 recovered to only $25\% \pm 3\%$ after 220 seconds (**Figure 2C and S2B**). In anaphase, KIF22-GFP
238 intensity immediately after bleaching was $17\% \pm 2\%$ of initial intensity, and intensity recovered to
239 $35\% \pm 6\%$ of initial intensity after 220 seconds (**Figure 2D and S2B**). This limited recovery
240 indicates that KIF22 stably associates with mitotic chromosomes. Pathogenic mutations did not
241 change these localization dynamics; recovery percentages in mitosis were also low in cells
242 expressing KIF22-GFP R149Q ($32 \pm 3\%$ of initial intensity in metaphase 220 seconds after
243 bleaching, $39 \pm 6\%$ in anaphase) (**Figure 2F and 2G**) and KIF22-GFP V475G ($29 \pm 2\%$ of initial
244 intensity in metaphase, $35 \pm 6\%$ in anaphase) (**Figure 2I and 2J**). These data indicate that
245 pathogenic mutations do not alter the localization of KIF22 to chromosomes and spindle
246 microtubules, and do not alter KIF22 localization dynamics in interphase, metaphase, or
247 anaphase.

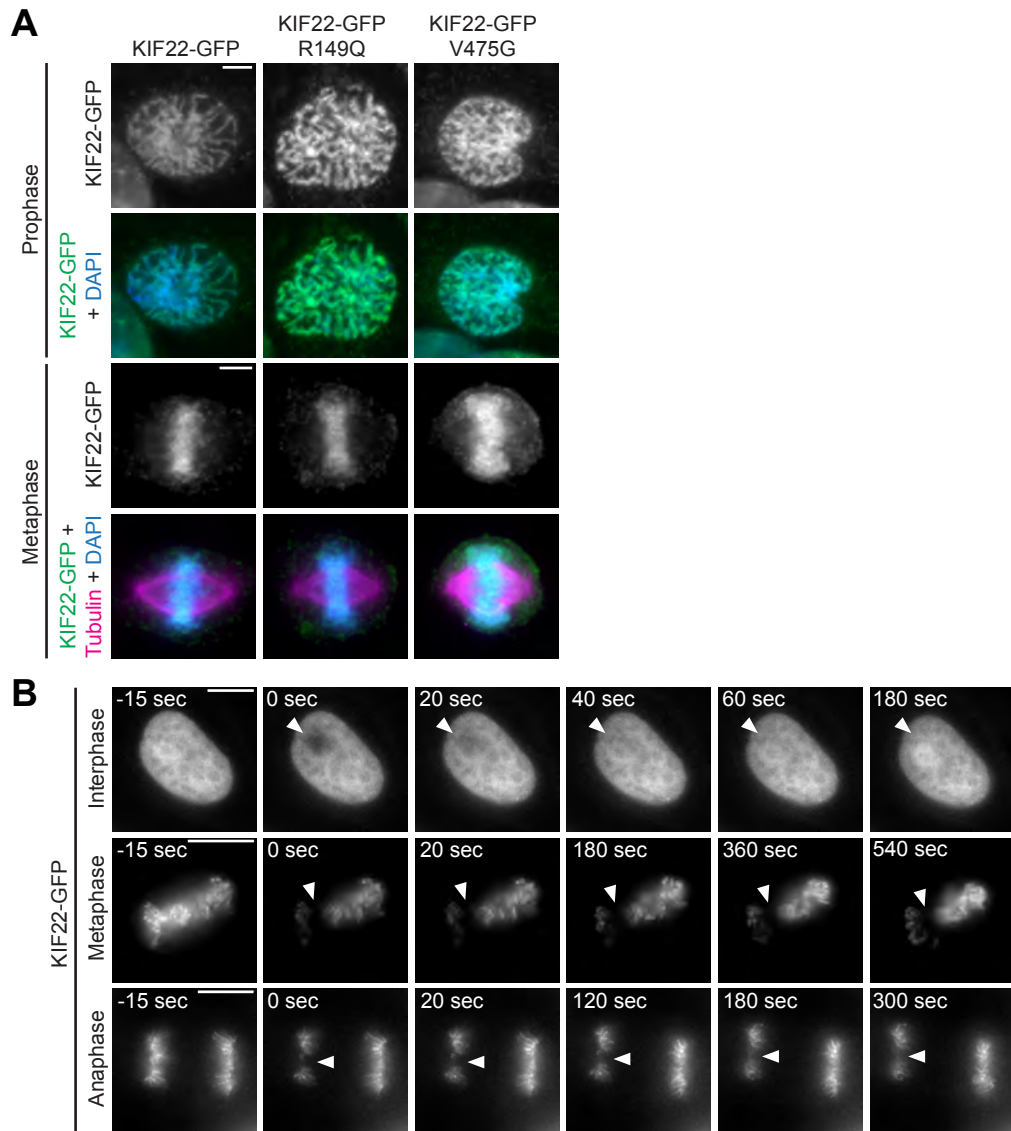
Figure 2



248 **Figure 2. Pathogenic mutations in KIF22 do not disrupt the localization of the motor.**

249 **(A)** Immunofluorescence images of HeLa-Kyoto cells expressing KIF22-GFP constructs in
250 prophase (top two rows) and metaphase (bottom two rows). KIF22-GFP was visualized using an
251 anti-GFP antibody. Images are maximum intensity projections in z of five frames at the center of
252 the spindle (metaphase cells) or maximum intensity projections in z of two frames (prophase
253 cells). Fixed approximately 24 hours after treatment with doxycycline to induce expression. Scale
254 bars 5 μm . **(B-J)** Fluorescence recovery after photobleaching (FRAP) of KIF22-GFP (B-D), KIF22-
255 GFP R149Q (E-G), and KIF22-GFP V475G (H-J) in interphase nuclei (B, E, H) or on metaphase
256 (C, F, I) or anaphase (D, G, J) chromosomes. Bleaching occurred at time zero. Thin lines are
257 traces from individual cells and thick lines represent means. Intensity values are normalized to
258 the KIF22-GFP intensity in the first imaged frame before bleaching. 6-14 cells from 3-5
259 experiments per condition.

Supplemental Figure 2



260 **Supplemental Figure 2. Pathogenic mutations in KIF22 do not disrupt the localization of**
261 **the motor in RPE-1 cells.**

262 **(A)** Immunofluorescence images of RPE-1 cells expressing KIF22-GFP constructs in prophase
263 (top two rows) and metaphase (bottom two rows). KIF22-GFP was visualized using an anti-GFP
264 antibody. Images are maximum intensity projections in z of five frames at the center of the spindle
265 (metaphase cells) or maximum intensity projections in z of three frames (prophase cells). Fixed
266 approximately 18 hours after treatment with doxycycline to induce expression. Scale bars 5 μm .

267 **(B)** Time-lapse images of fluorescence recovery after photobleaching (FRAP) in HeLa-Kyoto cells
268 expressing KIF22-GFP. Bleaching occurred at time zero, and arrowheads indicate bleached area.
269 Scale bars 10 μm . Images are representative of 3 or more experiments.

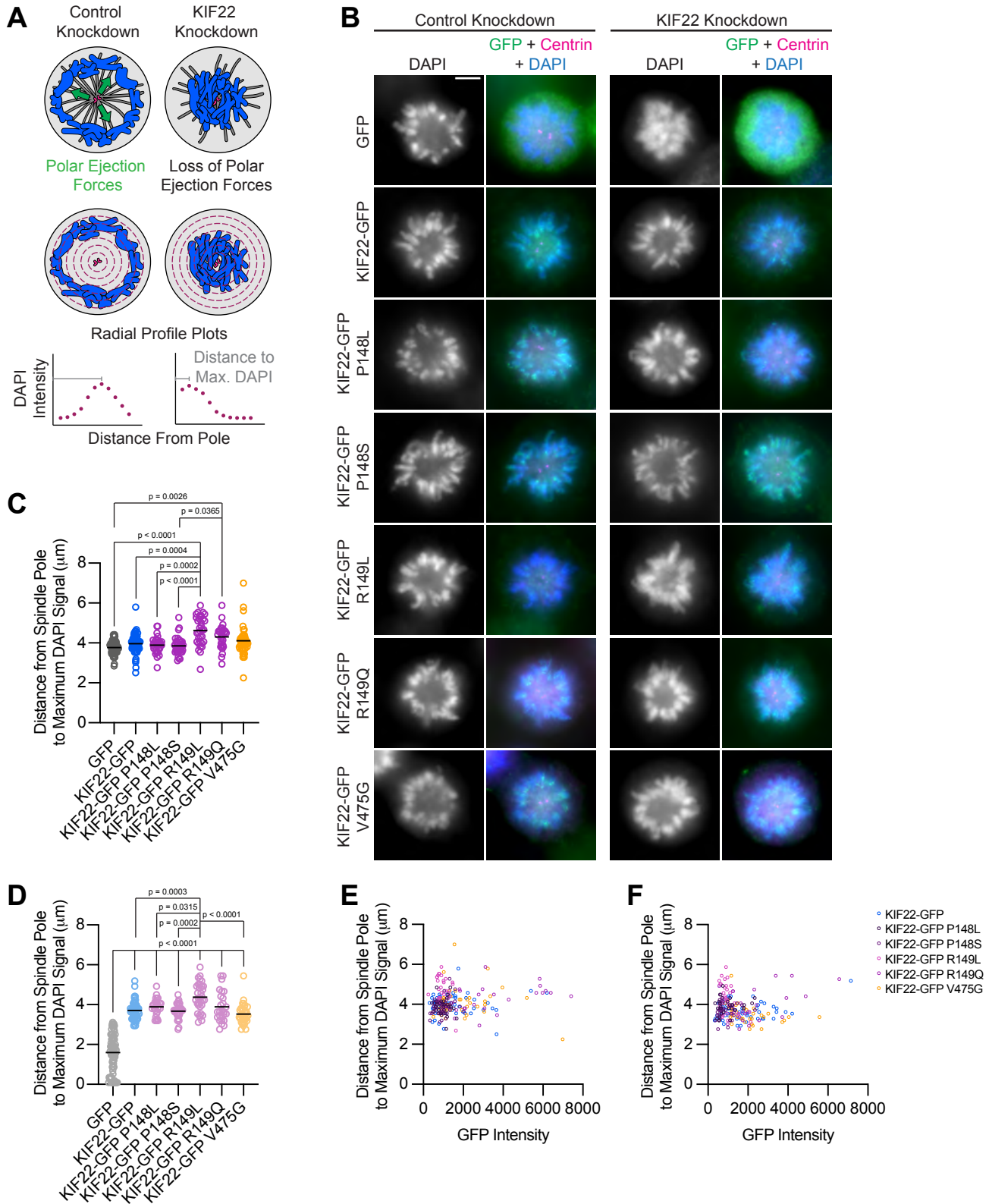
270 **Mutations do not reduce polar ejection forces**

271 In prometaphase and metaphase, KIF22 contributes to chromosome congression and
272 alignment by generating polar ejection forces (Levesque and Compton 2001; Stumpff et al. 2012;
273 Brouhard and Hunt 2005; Wandke et al. 2012). In cells treated with monastrol to inhibit Eg5/KIF11
274 and generate monopolar spindles, polar ejection forces push chromosomes away from a single
275 central spindle pole (Levesque and Compton 2001) (**Figure 3A**). A loss of KIF22 function causes
276 chromosomes to collapse in towards the pole in this system (Levesque and Compton 2001)
277 (**Figure 3A**). To determine whether overexpression of KIF22-GFP with pathogenic mutations has
278 a dominant effect on polar ejection force generation, wild type or mutant KIF22-GFP-expressing
279 HeLa-Kyoto cells were treated with monastrol to induce mitotic arrest with monopolar spindles.
280 Relative polar ejection forces were compared by measuring the distance from the spindle pole to
281 the maximum DAPI signal (**Figure 3A**). Expression of mutant motor did not reduce polar ejection
282 forces (**Figure 3B and 3C**). Rather, expression of KIF22-GFP R149L and R149Q significantly
283 increased the distance from the pole to the maximum DAPI signal (R149L $4.6 \pm 0.13 \mu\text{m}$, R149Q
284 $4.3 \pm 0.11 \mu\text{m}$, GFP control $3.7 \pm 0.04 \mu\text{m}$, mean \pm SEM), indicating higher levels of polar ejection
285 forces in these cells.

286 The same assay was used to test whether mutant KIF22 could rescue polar ejection force
287 generation in cells depleted of endogenous KIF22. In control cells expressing GFP, depletion of
288 endogenous KIF22 resulted in the collapse of chromosomes towards the pole (**Figure 3B**), and
289 the distance from the pole to the maximum DAPI signal was reduced to $1.6 \pm 0.11 \mu\text{m}$, indicating
290 a loss of polar ejection forces (**Figure 3D**). This reduction was not observed in cells expressing
291 wild type or mutant KIF22-GFP, demonstrating that KIF22-GFP with pathogenic mutations is
292 capable of generating polar ejection forces (**Figure 3B and 3D**). In cells transfected with control
293 siRNA and cells depleted of endogenous KIF22, polar ejection force levels did not depend on
294 KIF22-GFP expression levels (**Figure 3E and 3F**).

295 Together, the localization of mutant KIF22 and the ability of mutant KIF22 to generate
296 polar ejection forces indicate that pathogenic mutations P148L, P148S, R149L, R149Q, and
297 V475G do not result in a loss of KIF22 function during early mitosis.

Figure 3



298 **Figure 3. Pathogenic mutations in KIF22 do not reduce polar ejection forces.**

299 **(A)** Schematic of changes in chromosome positions resulting from loss of polar ejection forces.
300 In cells with monopolar spindles, both spindle poles (magenta) are positioned together and
301 chromosomes (blue) are pushed toward the cell periphery by polar ejection forces (green) (left).
302 In cells depleted of KIF22, polar ejection forces are reduced and chromosomes collapse in toward
303 the center of the cell (right). Relative polar ejection forces were quantified using radial profile plots
304 to measure the distance from the spindle pole to the maximum DAPI signal intensity. **(B)**
305 Immunofluorescence images of monopolar HeLa-Kyoto cells. KIF22-GFP was visualized using
306 an anti-GFP antibody. Fixed approximately 2-3 hours after treatment with monastrol and 24 hours
307 after siRNA transfection and treatment with doxycycline to induce expression. Scale bar 5 μm .
308 Images are representative of 3 or more experiments. **(C)** Distance from the spindle pole to the
309 maximum DAPI signal, a measure of relative polar ejection force level, in cells transfected with
310 control siRNA. 28-69 cells from 3-7 experiments per condition. **(D)** Distance from the spindle pole
311 to the maximum DAPI signal in cells transfected with KIF22 siRNA. 26-75 cells from 3-7
312 experiments per condition. For C-D, bars indicate means. p values from Brown-Forsythe and
313 Welch ANOVA with Dunnett's T3 multiple comparisons test. p values are greater than 0.05 for
314 comparisons without a marked p value. **(E-F)** Background-subtracted GFP intensity plotted
315 against the distance from the spindle pole to the maximum DAPI signal to assess dependence of
316 polar ejection force generation on expression levels in cells transfected with control siRNA (E)
317 (Pearson correlation coefficient 0.105, two-tailed p value 0.1031) or KIF22 siRNA (F) (Pearson
318 correlation coefficient -0.005, two-tailed p value 0.9427).

319 **KIF22 mutations disrupt anaphase chromosome segregation**

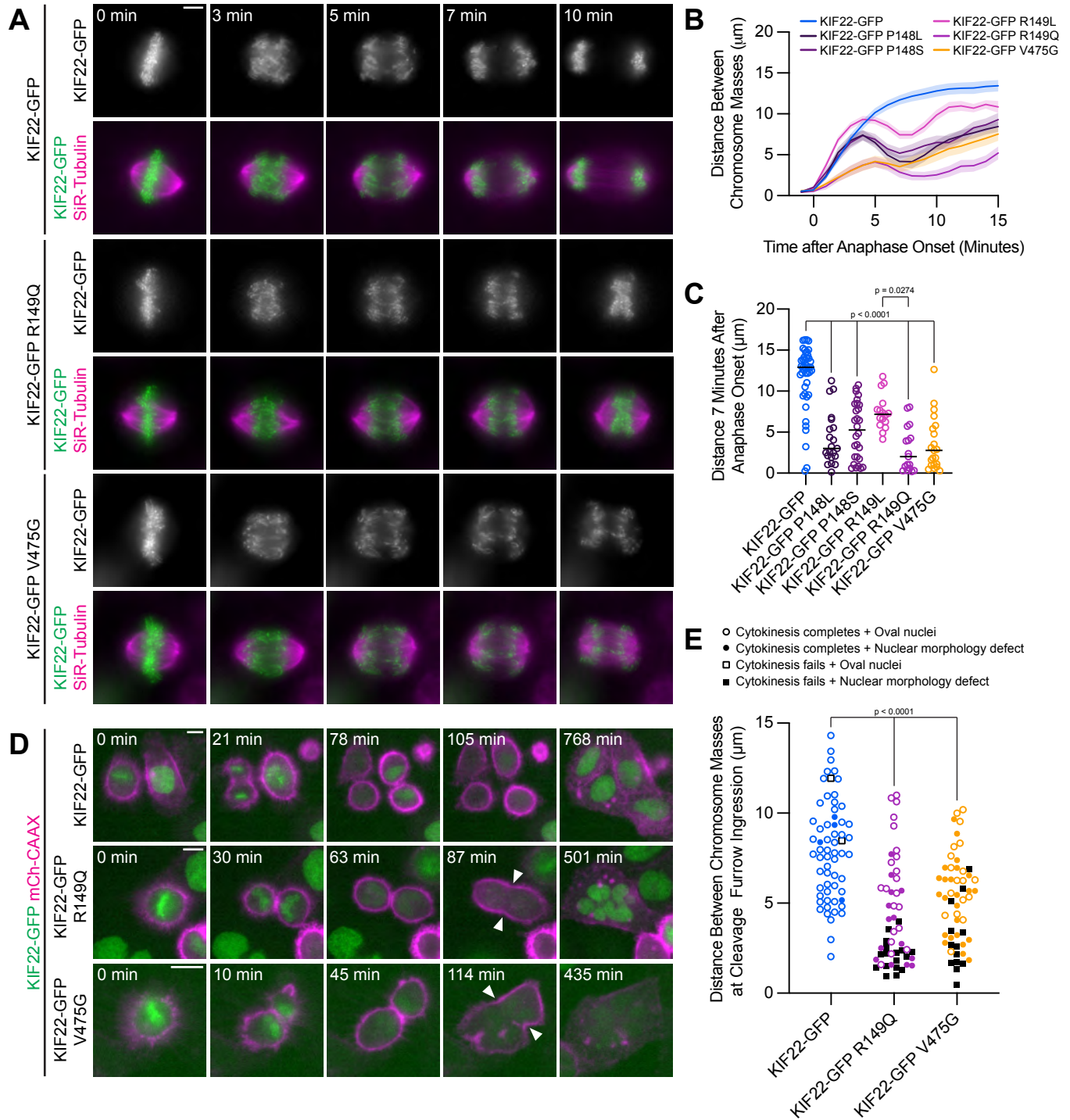
320 While pathogenic mutations did not disrupt the function of KIF22 in prometa- or
321 metaphase, HeLa-Kyoto cells expressing mutant KIF22-GFP exhibited defects in anaphase
322 chromosome segregation. In these cells, chromosomes did not move persistently towards the
323 spindle poles. Instead, chromosomes began to segregate, but then reversed direction and moved
324 back towards the center of the spindle or remained in the center of the spindle until
325 decondensation (**Figure 4A**). This phenotype was dominant and occurred in the presence of
326 endogenous KIF22. Recongression was quantified by measuring the distance between
327 separating chromosome masses as anaphase progressed. In cells expressing wild type KIF22-
328 GFP, this value increases steadily and then plateaus. Expression of mutant KIF22-GFP causes
329 the distance between chromosome masses to increase, then decrease as chromosomes
330 recondense, and then increase again as segregation continues (**Figure 4B**). Recongression
331 reduces the distance between chromosome masses 7 minutes after anaphase onset in cells
332 expressing KIF22-GFP with pathogenic mutations (median distance 2.0 – 7.2 μm) compared to
333 cells expressing wild type KIF22-GFP (median distance 12.9 μm) (**Figure 4C**). Defects in
334 anaphase chromosome segregation were also observed in RPE-1 cells expressing KIF22-GFP
335 R149Q or V475G (**Figure S3D, S3E, S3F**). This gain of function phenotype is consistent with a
336 lack of KIF22 inactivation in anaphase, resulting in a failure to suspend polar ejection force
337 generation.

338 If recongression is the result of increased KIF22 activity in anaphase, we would predict
339 that increased levels of KIF22-GFP expression would cause more severe anaphase chromosome
340 segregation defects. Indeed, plotting the distance between chromosome masses 7 minutes after
341 anaphase onset against mean GFP intensity for each HeLa-Kyoto cell demonstrated that these
342 two values were correlated (Spearman correlation coefficient -0.6246, one-tailed p value <
343 0.0001) (**Figure S3A**). Considering only cells expressing lower levels of KIF22-GFP (mean
344 background subtracted intensity <100 arbitrary units) emphasized the differences in the distance
345 between chromosome masses as anaphase progressed between cells expressing wild type and
346 mutant motor (**Figure S3B, S3C**).

347 In a subset of HeLa-Kyoto cells, expression of KIF22-GFP with pathogenic mutations
348 caused cytokinesis failure (**Figure 4D**). In these cells, cleavage furrow ingression began, but did
349 not complete, resulting in a single daughter cell. The percentage of cells failing to complete
350 cytokinesis was approximately ten-fold higher in cells expressing mutant KIF22-GFP (R149Q
351 36%, V475G 25%) than in cells expressing wild type KIF22-GFP (3%). Additionally, the distance
352 between chromosome masses at the time of cleavage furrow ingression was reduced in cells

353 expressing KIF22-GFP R149Q or V475G, suggesting that the position of the chromosome
354 masses may be physically obstructing cytokinesis (**Figure 4E**). Consistent with this hypothesis,
355 cells that failed to complete cytokinesis tended to have lower distances between chromosome
356 masses than the distances measured in cells in which cytokinesis completed despite expression
357 of mutant KIF22-GFP (**Figure 4E**).

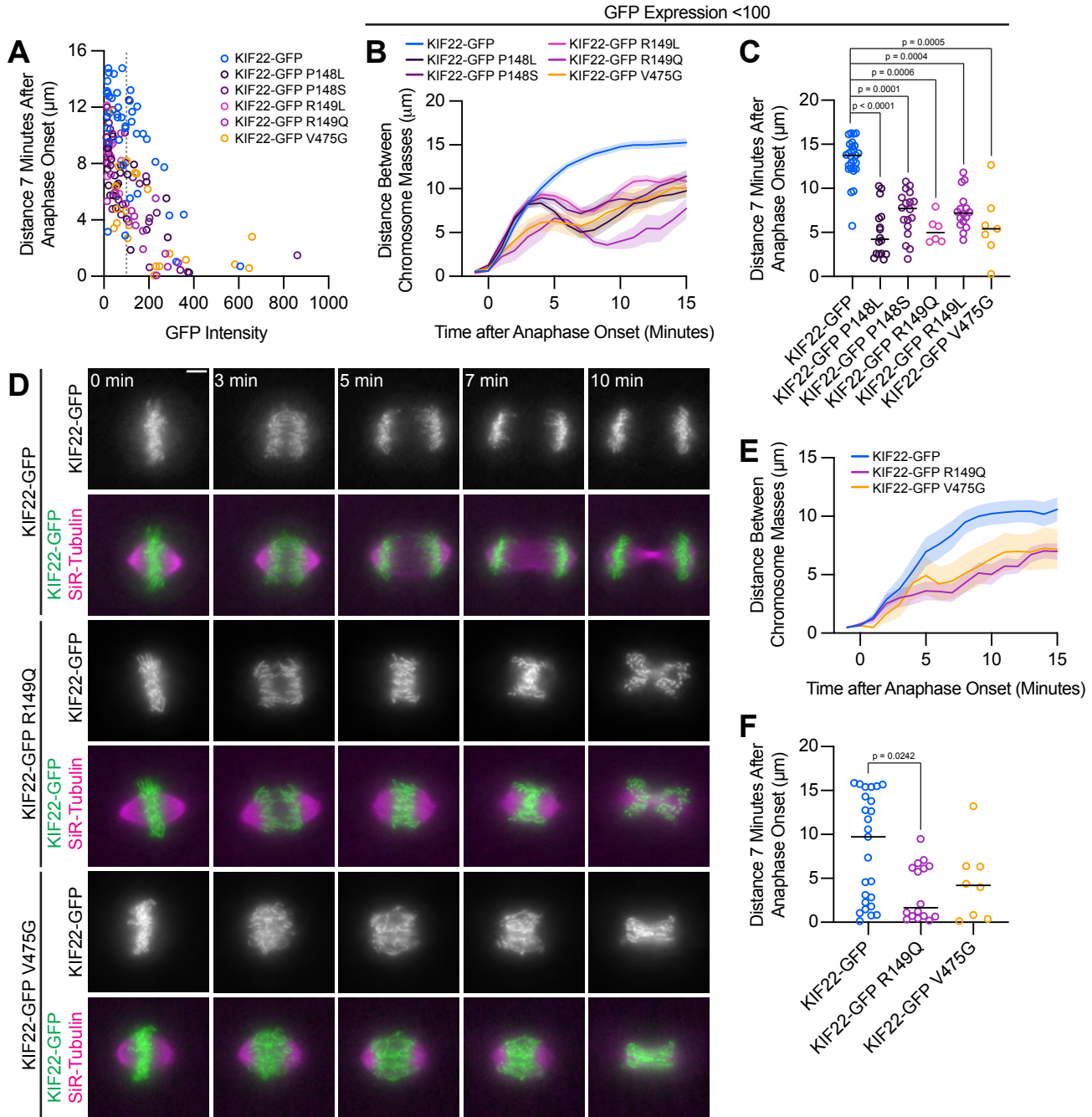
Figure 4



358 **Figure 4. Pathogenic mutations in KIF22 disrupt anaphase chromosome segregation.**

359 **(A)** Time-lapse images of dividing HeLa-Kyoto cells expressing KIF22-GFP R149Q or KIF22-GFP
360 V475G. Times indicate minutes after anaphase onset. Images are maximum intensity projections
361 in z through the entirety of the spindle. Imaged approximately 18 hours after treatment with
362 doxycycline to induce expression. Scale bar 5 μ m. Images are representative of 3 or more
363 experiments. **(B)** Distance between separating chromosome masses throughout anaphase in
364 HeLa-Kyoto cells. Lines represent the mean and the shaded area denotes SEM. 16-43 cells from
365 4-10 experiments per condition. **(C)** Distance between separating chromosome masses 7 minutes
366 after anaphase onset. Bars indicate medians. p values from Kruskal-Wallis test. p values are
367 greater than 0.05 for comparisons without a marked p value. 16-43 cells from 4-10 experiments
368 per condition. **(D)** Time-lapse images of dividing HeLa-Kyoto cells expressing mCherry (mCh)-
369 CAAX to visualize cell boundaries. Times indicate minutes after anaphase onset. Arrowheads
370 indicate cytokinesis failure. Imaged approximately 8 hours after treatment with doxycycline to
371 induce expression and 24-32 hours after transfection with mCh-CAAX. Scale bars 20 μ m. Images
372 are representative of 3 or more experiments. **(E)** Distance between chromosome masses at the
373 time of cleavage furrow ingression. p values from Kruskal-Wallis test. p values are greater than
374 0.05 for comparisons without a marked p value. 52-62 cells from 9-10 experiments per condition.

Supplemental Figure 3



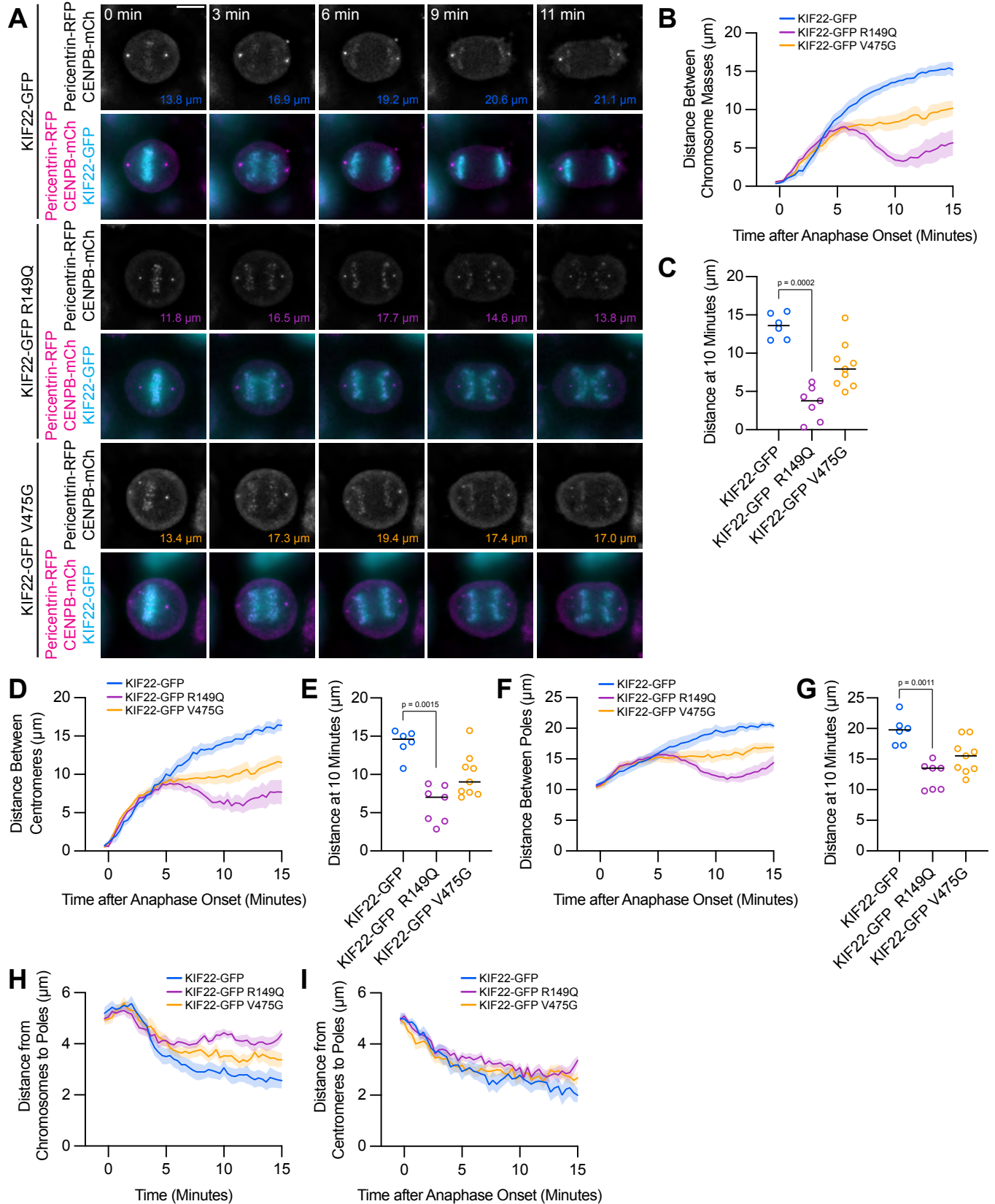
375 **Supplemental Figure 3. Anaphase recongression defects are KIF22-GFP expression level**
376 **dependent and disrupt chromosome segregation in RPE1 cells.**

377 **(A)** Background-subtracted GFP intensity plotted against the distance between separating
378 chromosome masses at 7 minutes to assess dependence of recongression on expression level
379 (Spearman correlation coefficient -0.6246, one-tailed p value < 0.0001). Grey dashed line
380 indicates mean background subtracted GFP intensity of 100. 16-43 cells from 4-10 experiments
381 per condition. **(B)** Distance between separating chromosome masses of cells expressing lower
382 levels of KIF22-GFP (mean background subtracted GFP intensity less than 100). Lines represent
383 the mean and the shaded area denotes SEM. 6-24 cells from 3-8 experiments per condition. **(C)**
384 Distance between separating chromosome masses 7 minutes after anaphase onset of cells
385 expressing lower levels of KIF22-GFP (mean background subtracted GFP intensity less than
386 100). Bars indicate medians. p values from Kruskal-Wallis test. p values are greater than 0.05 for
387 comparisons without a marked p value. 6-24 cells from 3-8 experiments per condition. **(D)** Time-
388 lapse images of dividing RPE-1 cells expressing KIF22-GFP R149Q or KIF22-GFP V475G.
389 Imaged approximately 12-18 hours after treatment with doxycycline to induce expression. Times
390 indicate minutes after anaphase onset. Images are maximum intensity projections in z through
391 the entirety of the spindle. Scale bar 5 μm . Images are representative of 3 or more experiments.
392 **(E)** Distance between separating chromosome masses throughout anaphase in RPE-1 cells.
393 Lines represent the mean and the shaded area denotes SEM. 8-25 cells from 6-7 experiments
394 per condition. **(F)** Distance between separating chromosome masses 7 minutes after anaphase
395 onset in RPE-1 cells. Bars indicate medians. p value from Kruskal-Wallis test. p values are greater
396 than 0.05 for comparisons without a marked p value. 8-25 cells from 6-7 experiments per
397 condition.

398 **Mutations disrupt the separation of the spindle poles in anaphase**

399 Anaphase chromosome segregation requires both that chromosome arms and
400 centromeres move towards the spindle poles (anaphase A) (Asbury 2017) and that the spindle
401 poles move away from one another (anaphase B) (Ris 1949). To test whether the activity of
402 mutant KIF22 in anaphase affects one or both of these processes, anaphase was imaged in HeLa-
403 Kyoto cells expressing fluorescent markers for the poles (pericentrin-RFP) and centromeres
404 (CENPB-mCh) (**Figure 5A**). The reduced distance between separating chromosome masses
405 seen in these cells (**Figure 5B, 5C**) was compared to the distances between the centromeres
406 (**Figure 5D, 5E**) and the distances between the poles (**Figure 5F, 5G**) as anaphase progressed.
407 The distances between all three structures showed the same trend: in cells expressing wild type
408 KIF22-GFP, the distance between chromosome masses, between centromeres, and between the
409 spindle poles increased throughout the measured time interval in anaphase. Pathogenic
410 mutations altered the movements of all three structures (**Figure 5B, 5D, 5F**). The distance
411 between chromosome masses, between centromeres, and between the spindle poles 10 minutes
412 after anaphase onset was significantly reduced in cells expressing KIF22-GFP R149Q (**Figure**
413 **5C, 5E, 5G**). In cells expressing KIF22-GFP V475G, the same trend was observed, but the
414 reductions in distance were not statistically significant. Comparing the distance between
415 chromosome masses and the spindle pole within each half spindle (**Figure 5H**) with the distance
416 between centromeres and the spindle pole in the same half spindles (**Figure 5I**) demonstrated
417 that expression of mutant KIF22 more potently reduced the segregation of chromosome arms
418 than centromeres, consistent with continued generation of polar ejection forces in anaphase. This
419 suggests that pathogenic mutations in KIF22 affect anaphase A by altering the movement of
420 chromosome arms, but not the shortening of the k-fibers, and affect anaphase B by altering
421 spindle pole separation.

Figure 5



422 **Figure 5. Mutations disrupt the separation of spindle poles in anaphase.**

423 **(A)** Time-lapse images of dividing HeLa-Kyoto cells expressing pericentrin-RFP to mark the
424 spindle poles and CENPB-mCh to mark centromeres. Times indicate minutes after anaphase
425 onset. Colored distances in the bottom right of each greyscale image indicate the distance
426 between the spindle poles in the image. Images are maximum intensity projections in z through
427 the entirety of the spindle. Imaged approximately 24 hours after transfection and 12-18 hours after
428 treatment with doxycycline to induce expression. Images depicting pericentrin-RFP and CENPB-
429 mCh signal were background subtracted by duplicating each frame, applying a gaussian blur
430 (sigma 30 pixels), and subtracting this blurred image from the original. Scale bar 10 μm . Images
431 are representative of 3 or more experiments. **(B)** Distance between separating chromosome
432 masses throughout anaphase in HeLa-Kyoto cells. Lines represent the mean and the shaded
433 area denotes SEM. **(C)** Distance between separating chromosome masses 10 minutes after
434 anaphase onset in HeLa-Kyoto cells. Bars indicate medians. **(D)** Distance between centromeres
435 (CENPB-mCh) throughout anaphase in HeLa-Kyoto cells. Lines represent the mean and the
436 shaded area denotes SEM. **(E)** Distance between centromeres 10 minutes after anaphase onset
437 in HeLa-Kyoto cells. Bars indicate medians. **(F)** Distance between spindle poles (pericentrin-RFP)
438 throughout anaphase in HeLa-Kyoto cells. Lines represent the mean and the shaded area
439 denotes SEM. **(G)** Distance between spindle poles 10 minutes after anaphase onset in HeLa-
440 Kyoto cells. Bars indicate medians. Measurements from the same cells (6-9 cells from 3
441 experiments per condition) are shown in B-G. For C, E, and G, p values from Kruskal-Wallis test.
442 p values are greater than 0.05 for comparisons without a marked p value. **(H)** Distance between
443 chromosome masses and spindle poles throughout anaphase in HeLa-Kyoto cells. Lines
444 represent the mean and the shaded area denotes SEM. **(I)** Distance between centromeres and
445 spindle poles throughout anaphase in HeLa-Kyoto cells. Lines represent the mean and the
446 shaded area denotes SEM. Measurements from the same cells (12-18 half-spindle
447 measurements from 3 experiments per condition) as in B-G are shown in H and I.

448 **Division of cells expressing KIF22 with pathogenic mutations results in daughter cells with**
449 **abnormally shaped nuclei**

450 To understand the consequences of the observed defects in anaphase chromosome
451 segregation, we examined the daughter cells produced by the division of cells expressing KIF22-
452 GFP with pathogenic mutations. In these cells, the nuclei are lobed and fragmented (**Figure 6A**).
453 The percentage of divisions resulting in nuclear morphology defects was approximately ten-fold
454 higher than in control cells (KIF22-GFP 6%, KIF22-GFP R149Q 64%, KIF22-GFP V475G 68%)
455 when live divisions were observed (**Figure 4E**). To further quantify this phenotype, the solidity of
456 fixed cell nuclei (the ratio of the area of each nucleus to the area of the convex shape that would
457 enclose it) was measured. A perfectly oval nucleus would have a solidity value of one. Solidity
458 values were reduced in cells expressing KIF22-GFP with pathogenic mutations (**Figure 6B**),
459 indicating that these cells had more irregularly shaped nuclei. This reduction in solidity was
460 dominant and occurred both in the presence of endogenous KIF22 and when endogenous KIF22
461 was depleted via siRNA knockdown. Using the fifth percentile solidity of control cells (control
462 knockdown, GFP expression) as a cut-off, 44-63% of cells expressing mutant KIF22-GFP had
463 abnormally shaped nuclei 24 hours after treatment with doxycycline to induce expression of
464 KIF22-GFP (**Figure 6C**). Expression of wild type KIF22-GFP also resulted in a small increase in
465 the percentage of cells with abnormally shaped nuclei (12%). This percentage was reduced when
466 endogenous KIF22 was depleted (7%), consistent with nuclear morphology defects resulting from
467 an increase in KIF22 activity.

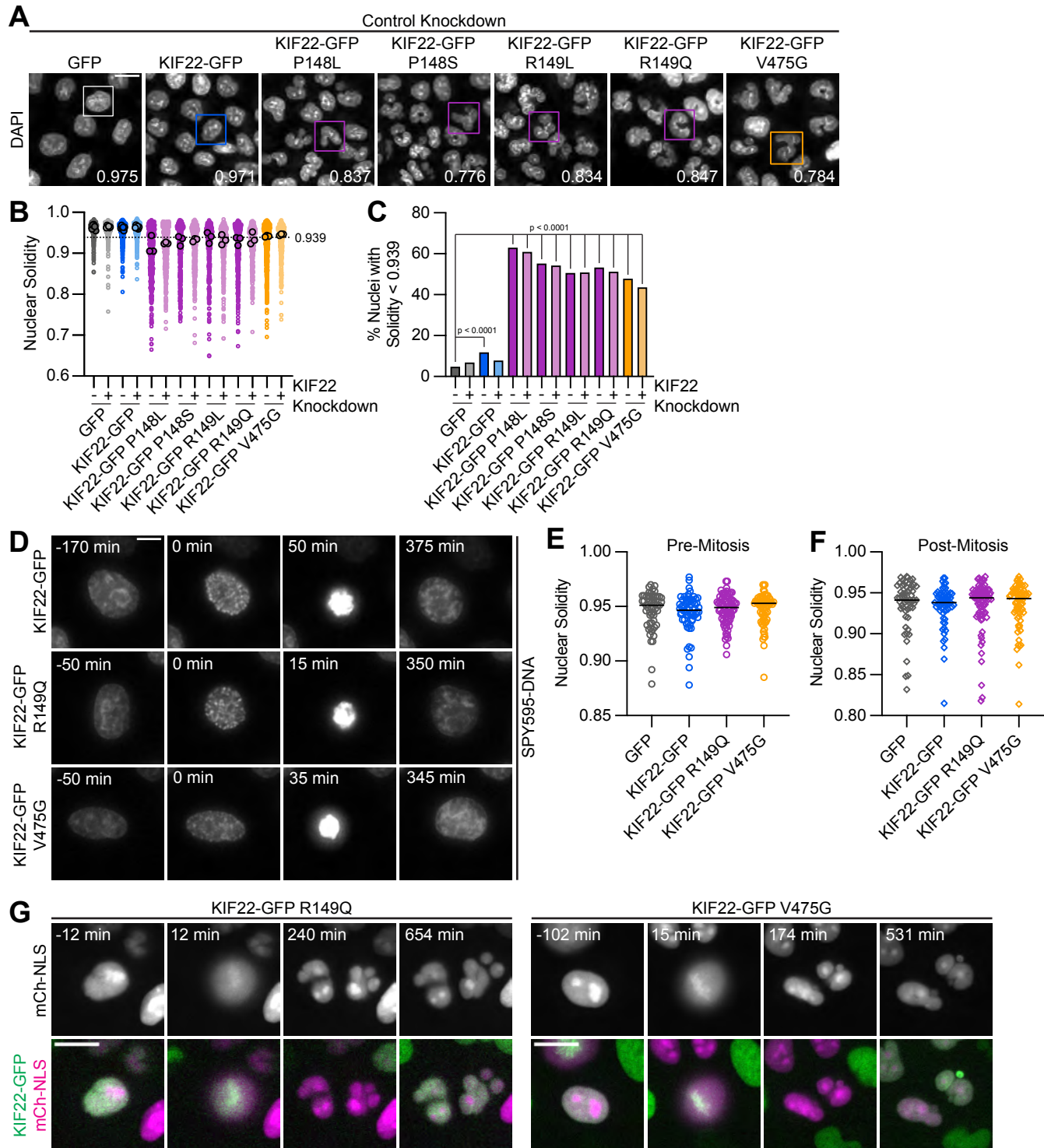
468 Expression of KIF22-GFP with pathogenic mutations also caused abnormally shaped
469 nuclei in RPE-1 cells (**Figure S4A**). The solidity of nuclei in cells expressing mutant KIF22-GFP
470 was reduced (**Figure S4B**), and 40-49% of RPE-1 cells expressing mutant KIF22-GFP had
471 abnormally shaped nuclei, again defined as a solidity value less than the fifth percentile of control
472 cells (**Figure 4C**). In RPE-1 cells, expression of wild type KIF22-GFP resulted in a higher
473 percentage of cells with abnormally shaped nuclei (18% in control knockdown cells, 15% with
474 KIF22 knockdown) than was seen in HeLa-Kyoto cells. This may be a result of the higher
475 expression level of KIF22-GFP in the RPE-1 inducible cell lines (**Figure S1I, S1K**).

476 To determine whether these nuclear morphology defects depended on the ability of KIF22
477 to generate forces within the mitotic spindle, cells were treated with nocodazole to depolymerize
478 microtubules and reversine to silence the spindle assembly checkpoint, allowing cells to enter
479 and exit mitosis without assembling a spindle or segregating chromosomes (Samwer et al. 2017;
480 Serra-Marques et al. 2020) (**Figure 6D**). The solidity of nuclei was measured before
481 chromosomes condensed (**Figure 6E**) and after mitotic exit (**Figure 6F**). At both time points, there

482 was no difference in nuclear shape between control cells and cells expressing KIF22-GFP with
483 pathogenic mutations, indicating that the effects of mutations on nuclear structure are spindle-
484 dependent.

485 The effect of nuclear morphology defects on daughter cell fitness may partially depend on
486 whether the nuclear envelopes of abnormally shaped nuclei are intact. The expression of mCherry
487 (mCh) with a nuclear localization signal (NLS) indicated that even highly lobed and fragmented
488 nuclei in cells expressing mutant KIF22-GFP are capable of retaining nuclear-localized proteins
489 **(Figure 6G)**. This suggests that the nuclear envelopes of these abnormally shaped nuclei are still
490 intact enough to function as a permeability barrier (Hatch et al. 2013).

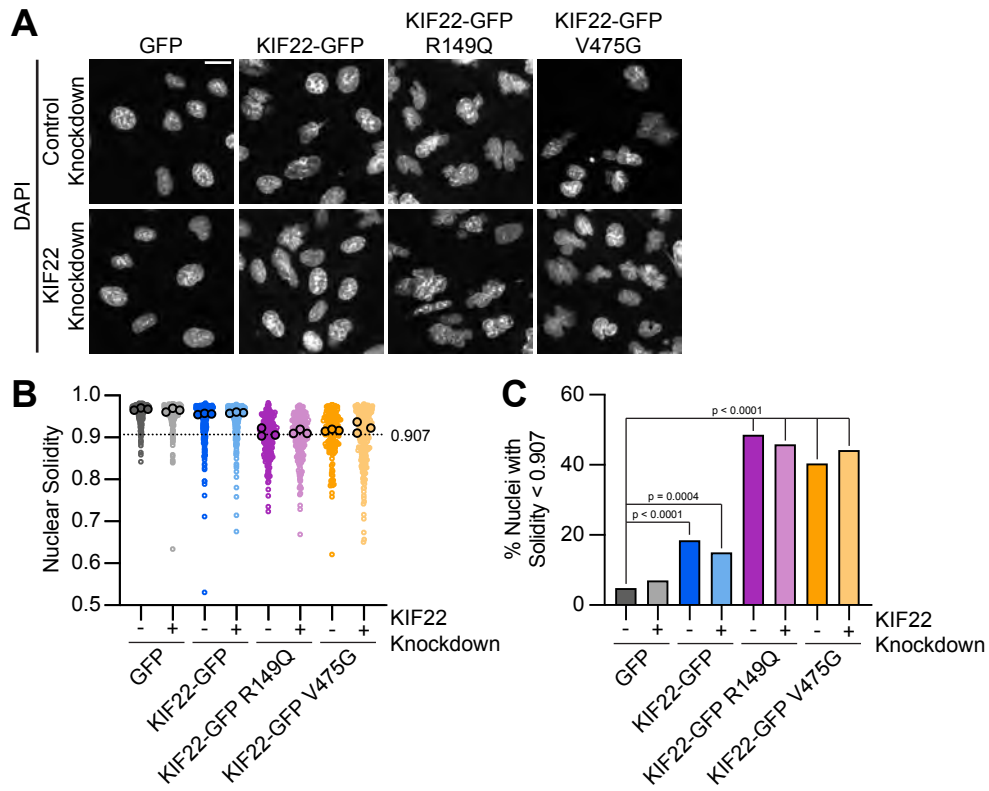
Figure 6



491 **Figure 6: Division of cells expressing KIF22 with pathogenic mutations results in daughter**
492 **cells with abnormally shaped nuclei.**

493 **(A)** DAPI stained nuclei of cells expressing KIF22 with pathogenic mutations. Values in the bottom
494 right of each image indicate the solidity of the boxed nucleus. Fixed approximately 24 hours after
495 treatment with doxycycline to induce expression. Scale bar 20 μm . Images are representative of
496 3 or more experiments. **(B)** Measured solidity of nuclei in HeLa-Kyoto cell lines. Small circles
497 represent the solidity of individual nuclei, and large circles with black outlines indicate the median
498 of each experiment. A dashed line marks a solidity value of 0.939, the fifth percentile of solidity
499 for control cells transfected with control siRNA and expressing GFP. **(C)** Percentage of nuclei with
500 abnormal shape, indicated by a solidity value less than 0.939, the fifth percentile of control (control
501 knockdown, GFP expression) cell solidity. A chi-square test of all data produced a p value <
502 0.0001. Plotted p values are from pairwise post-hoc chi-square tests comparing control (control
503 knockdown, GFP expression) cells to each other condition. Applying the Bonferroni correction for
504 multiple comparisons, a p value of less than 0.00385 was considered significant. p values are
505 greater than 0.00385 for comparisons without a marked p value. Data in (B) and (C) represent
506 336-1045 cells from 3-6 experiments per condition. **(D)** Time-lapse images of HeLa-Kyoto cells
507 treated with nocodazole and reversine and stained with SPY595-DNA to visualize chromosomes.
508 Time indicates the number of minutes before or after chromosome condensation. Images are
509 maximum intensity projections in z of two focal planes, one at the level of interphase nuclei and
510 one at the level of mitotic chromosomes. Imaged approximately 8 hours after treatment with
511 doxycycline to induce expression, 1.5-2 hours after treatment with SPY595-DNA, and 0.5-1 hour
512 after treatment with nocodazole and reversine. Scale bar 10 μm . Images are representative of 3
513 or more experiments. **(E)** Nuclear solidity of HeLa-Kyoto cells treated with nocodazole and
514 reversine. Measurements were made 15 minutes before chromosome condensation. **(F)** Nuclear
515 solidity of HeLa-Kyoto cells treated with nocodazole and reversine. Measurements were made
516 100 minutes after chromosome decondensation. Data in (E) and (F) represent 56-76 cells from 3
517 experiments per condition. For (E) and (F), bars indicate medians, and the Kruskal-Wallis test
518 indicated no significant difference between groups. **(G)** Time-lapse images of HeLa-Kyoto cells
519 expressing mCherry (mCh)-NLS to assess nuclear envelope integrity. Times indicate minutes
520 before or after chromosome condensation. Imaged approximately 8 hours after treatment with
521 doxycycline to induce expression and 24 hours after transfection with mCh-CAAX. Scale bar 20
522 μm . Images are representative of 3 or more experiments.

Supplemental Figure 4



523 **Supplemental Figure 4: Mutations cause abnormally shaped nuclei in RPE1 cells.**

524 **(A)** DAPI-stained nuclei of RPE-1 cells expressing KIF22-GFP with pathogenic mutations. Fixed
525 approximately 24 hours after treatment with doxycycline to induce expression. Scale bar 20 μm .
526 Images are representative of 3 or more experiments. **(B)** Measured solidity of nuclei in RPE-1 cell
527 lines. Small circles represent the solidity of individual nuclei, and large circles with black outlines
528 indicate the median of each experiment. A dashed line marks a solidity value of 0.907, the fifth
529 percentile of solidity for control cells transfected with control siRNA and expressing GFP. **(C)**
530 Percentage of nuclei with abnormal shape, indicated by a solidity value less than 0.907, the fifth
531 percentile of control (control knockdown, GFP expression) cell solidity. A chi-square test of all
532 data produced a p value < 0.0001 . Plotted p values are from pairwise post-hoc chi-square tests
533 comparing control (control knockdown, GFP expression) cells to each other condition. Applying
534 the Bonferroni correction for multiple comparisons, a p value of less than 0.00714 was considered
535 significant. p values are greater than 0.00714 for comparisons without a marked p value. Data in
536 (B) and (C) represent 146-244 cells from 3 experiments per condition.

537 **Proliferation is reduced in cells expressing KIF22 with pathogenic mutations**

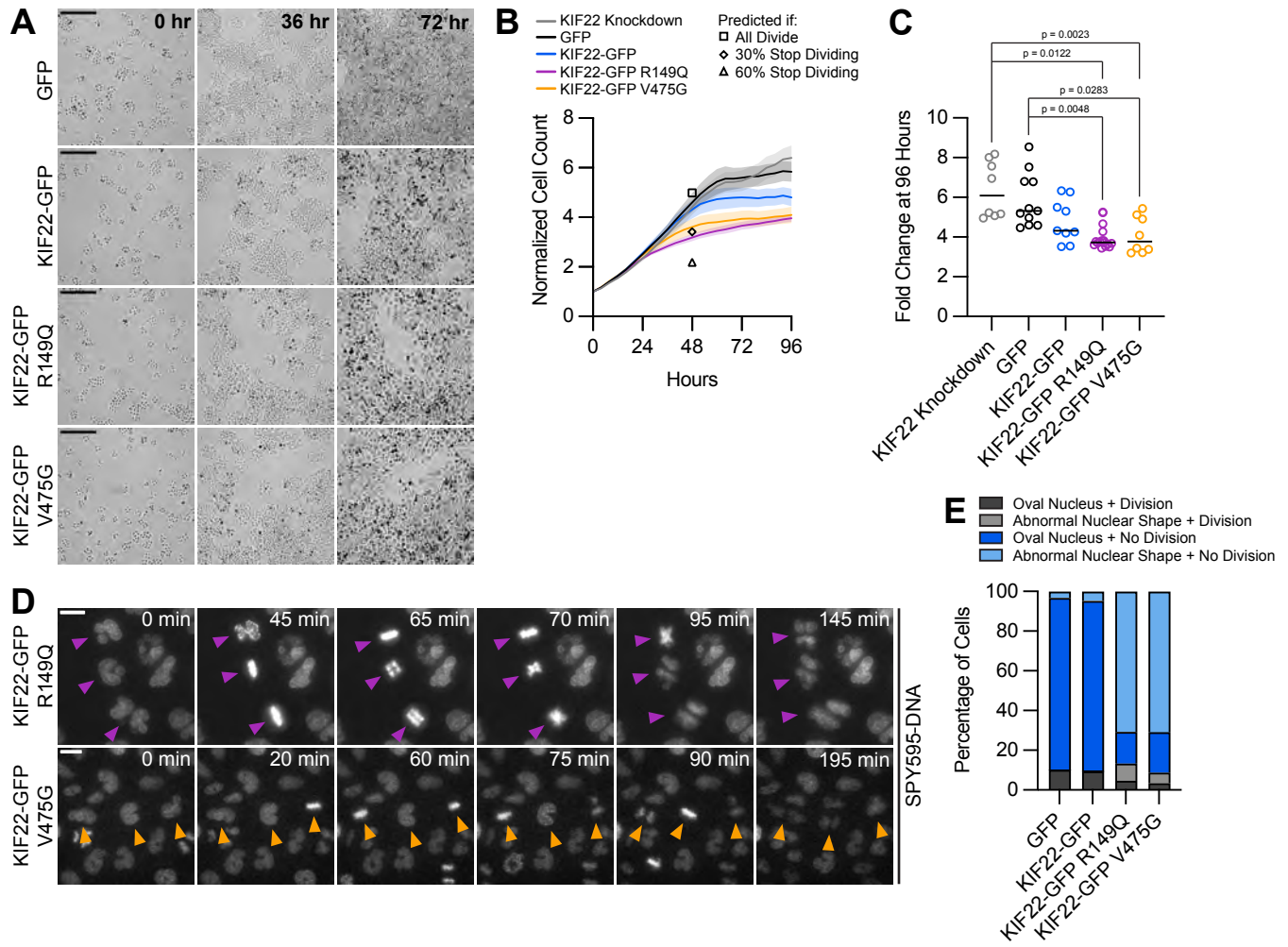
538 If defects in anaphase chromosome segregation and nuclear morphology affect cellular
539 function, they may impact the ability of cells to proliferate. To test this, HeLa-Kyoto cells
540 expressing KIF22-GFP with pathogenic mutations were imaged over 96 hours to count the
541 numbers of cells over time (**Figure 7A**). The growth rates of cells expressing mutant KIF22 were
542 reduced (**Figure 7B**). After 96 hours, the fold change in cell number was reduced by
543 approximately 30% for cells expressing KIF22-GFP with pathogenic mutations (GFP control
544 median 5.3, KIF22-GFP R149Q 3.7, KIF22-GFP V475G 3.8) (**Figure 7C**).

545 To consider what might be limiting the proliferation rate of cells expressing mutant KIF22-
546 GFP, predictions for proliferation rate based on the observed rates of nuclear morphology defects
547 and cytokinesis failure were calculated. For these purposes, only data from the first 48 hours of
548 the proliferation assay were used, as cell growth rates plateaued after this timepoint. The doubling
549 time of control HeLa-Kyoto cells expressing GFP was calculated to be 20.72 hours in these
550 experiments, which is consistent with published data (Y. Liu et al. 2018). Using this doubling rate,
551 assuming exponential growth, and assuming every cell divides, the normalized cell count at 48
552 hours (normalized to a starting cell count of 1) was predicted to be 4.98. This is close to the
553 experimental 48-hour cell count for control cells (4.60), and higher than the experimental 48-hour
554 cell count for cells expressing KIF22-GFP R149Q (3.13) or V475G (3.60), as these cell lines have
555 reduced proliferation (**Figure 7B, square**). If one assumed that cells with abnormally shaped
556 nuclei stop dividing, given that approximately 60% of mutant KIF22-GFP cell divisions result in
557 abnormally shaped nuclei (**Figure 4E**), the predicted cell count at 48 hours would be 2.18 (**Figure**
558 **7B, triangle**). This is lower than the experimental cell count for cells expressing mutant KIF22-
559 GFP, suggesting that cells with abnormally shaped nuclei must be capable of additional divisions.
560 If, instead, one assumed that only cells that fail cytokinesis (30% of cells (**Figure 4E**)) stop
561 dividing, the predicted cell count would be 3.42 (**Figure 7B, diamond**). This value is consistent
562 with the experimental 48-hour cell count for cells expressing KIF22-GFP with pathogenic
563 mutations (3.13 – 3.60), suggesting the rate of cytokinesis failure may limit the rate of proliferation
564 in these cells. Consistent with this possibility, an increased number of large cells that may have
565 failed cytokinesis are visible in proliferation assay images at 72 hours (**Figure 7A**).

566 To test the prediction that cells with nuclear morphology defects are capable of division,
567 KIF22-GFP expression was induced approximately 24 hours before imaging to generate a
568 population of cells with abnormally shaped nuclei. Division of these cells was observed (**Figure**
569 **7D**), demonstrating that nuclear morphology defects do not prevent subsequent divisions. The
570 percentage of cells that divided over the course of this experiment was not reduced in cells

571 expressing KIF22-GFP with pathogenic mutations despite the abnormal nuclear morphology of
572 cells in those populations (**Figure 7E**).

Figure 7



573 **Figure 7: Proliferation is reduced in cells expressing KIF22 with pathogenic mutations.**

574 **(A)** Time-lapse bright field images of HeLa-Kyoto cells to assess proliferation rate. Scale bar 500
575 μm . Images are representative of 3 or more experiments. **(B)** Proliferation rates measured using
576 automated bright field imaging. Lines represent the mean cell count, normalized to the number of
577 cells at 0 hours, and the shaded area denotes SEM. Black outlined shapes indicate the predicted
578 cell count for cell lines expressing pathogenic mutations at 48 hours if every cell doubled every
579 20.72 hours (the doubling time measured from 48 hours of control cell proliferation) (square), if
580 the rate of cytokinesis failure limited proliferation and 30% of cells did not divide (diamond), and
581 if the rate of nuclear morphology defects limited proliferation and 60% of cells did not divide
582 (triangle). **(C)** Fold change of normalized cell counts after 96 hours. Bars indicate medians. p
583 values from Kruskal-Wallis test. p values are greater than 0.05 for comparisons without a marked
584 p value. Data in (B) and (C) represent 8-16 technical replicates from 4 experiments per condition.
585 **(D)** Time-lapse imaging of HeLa-Kyoto cells treated with doxycycline for 24 hours to induce
586 expression of KIF22-GFP with pathogenic mutations and stained with SPY595-DNA. Arrowheads
587 indicate cells with abnormally shaped nuclei that divide. Images are maximum intensity
588 projections in z of two focal planes, one at the level of interphase nuclei and one at the level of
589 mitotic chromosomes. Scale bars 20 μm . Images are representative of 3 or more experiments.
590 **(E)** Nuclear morphology at the start of imaging (dark grey or blue, oval; light grey or blue; abnormal
591 morphology) and outcome (grey, cell divides during the experiment; blue, the cell does not divide).
592 The total number of dividing cells was compared between cell lines using the chi-square test ($p <$
593 0.0001 across all conditions). Post-hoc chi-square tests comparing all conditions to one another
594 indicated that the proliferation rate of cells expressing KIF22-GFP R149Q is statistically different
595 than that of cells expressing GFP ($p = 0.0025$), KIF22-GFP ($p = 0.0003$), or KIF22-GFP V475G
596 ($p < 0.0001$). Applying the Bonferroni correction for multiple comparisons, a p value of less than
597 0.008 was considered significant. p values are greater than 0.008 for all other comparisons. 1890-
598 2611 cells from 4 experiments per condition.

599 **Mimicking phosphorylation of T463 phenocopies pathogenic mutations**

600 The phenotypes observed in cells expressing KIF22-GFP with pathogenic mutations
601 suggest that mutations may prevent inactivation of KIF22 in anaphase, and that polar ejection
602 forces in anaphase disrupt chromosome segregation. If this is the case, then preventing KIF22
603 inactivation would be predicted to phenocopy the pathogenic mutations. One mechanism by
604 which KIF22 activity is controlled is phosphorylation of T463: phosphorylation of this tail residue
605 is necessary for polar ejection force generation, and dephosphorylation at anaphase onset
606 contributes to polar ejection force suppression (Soeda et al. 2016). Therefore, we generated
607 HeLa-Kyoto inducible cell lines expressing KIF22-GFP with phosphomimetic (T463D) and
608 phosphonull (T463A) mutations to test whether preventing KIF22 inactivation in anaphase by
609 expressing the constitutively active T463D construct phenocopies the expression of KIF22-GFP
610 with pathogenic mutations. When treated with doxycycline, these cells expressed
611 phosphomimetic and phosphonull KIF22-GFP at levels comparable to those seen in cells lines
612 expressing KIF22-GFP with pathogenic mutations, which was approximately two- to three-fold
613 higher than the level of expression of endogenous KIF22 (**Figure S5A-D**).

614 To assess the activity of KIF22-GFP T463D and T463A in HeLa cells, polar ejection force
615 generation in monopolar spindles was measured (**Figure 8A**). In cells with endogenous KIF22
616 present, expression of KIF22-GFP T463D increased the distance from the spindle pole to the
617 maximum DAPI signal (GFP control $3.7 \pm 0.07 \mu\text{m}$, KIF22-GFP T463D 4.4 ± 0.12 , mean \pm SEM),
618 indicating increased polar ejection forces, consistent with phosphorylation of T463 activating
619 KIF22 in prometaphase (Soeda et al. 2016) (**Figure 8B**). Conversely, when endogenous KIF22
620 was depleted, expression of KIF22-GFP T463A was less able to rescue polar ejection force
621 generation (distance from the spindle pole to the maximum DAPI signal $3.0 \pm 0.08 \mu\text{m}$, mean \pm
622 SEM) than expression of wild type KIF22-GFP ($3.6 \pm 0.07 \mu\text{m}$) or KIF22-GFP T463D (3.7 ± 0.10
623 μm) (**Figure 8C**). Again, this is consistent with previous work demonstrating that KIF22
624 phosphorylation at T463 activates the motor for prometaphase polar ejection force generation
625 (Soeda et al. 2016), although the reduction in polar ejection forces seen with KIF22-GFP T463A
626 rescue is less severe in our system, possibly due to differences in cell type, level of depletion of
627 endogenous KIF22, or the method used to quantify polar ejection forces.

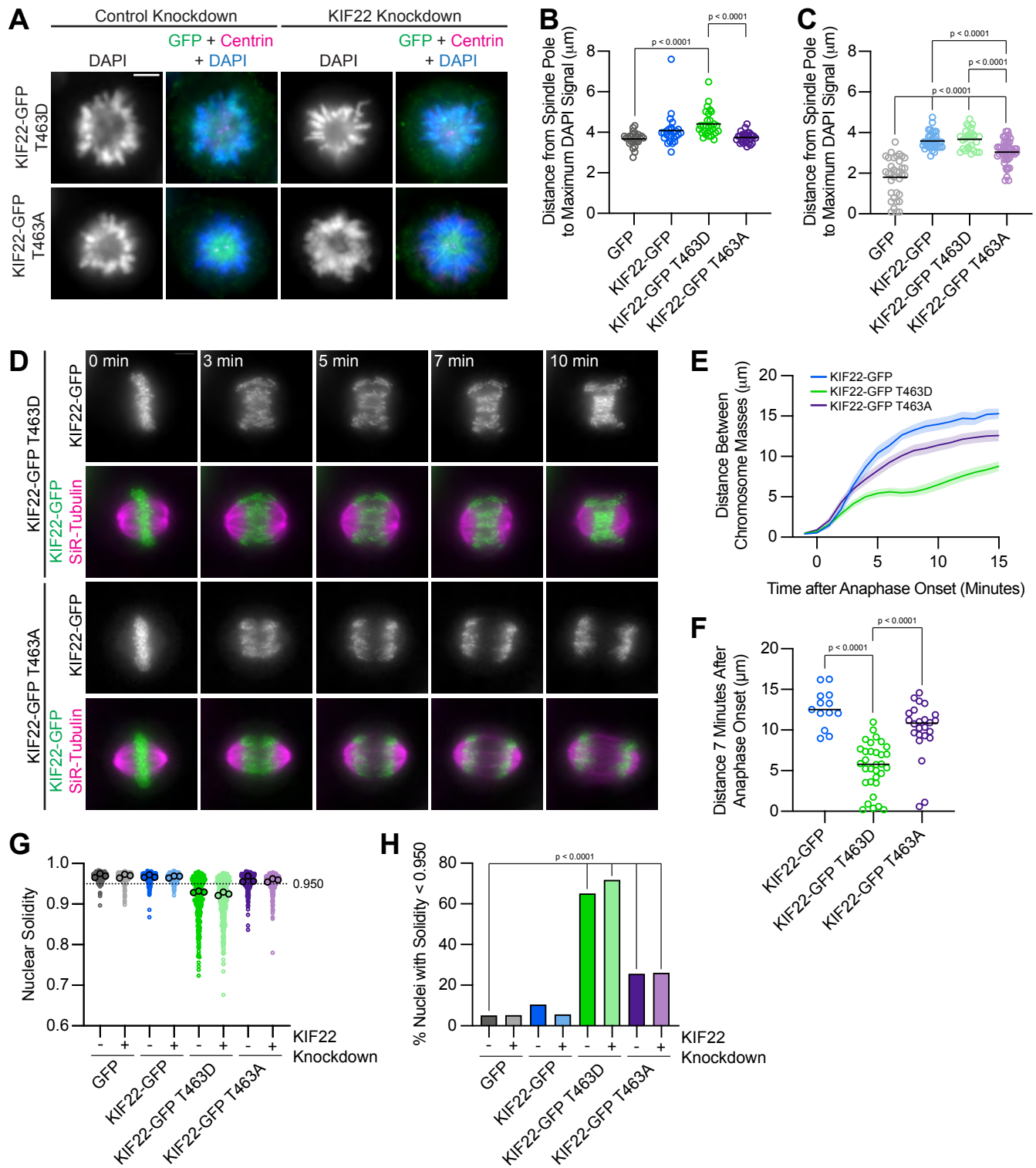
628 In anaphase, expression of phosphomimetic KIF22-GFP T463D, but not phosphonull
629 KIF22-GFP T463A, caused chromosome recongression (**Figure 8D, 8E**). The distance between
630 chromosome masses at 7 minutes was reduced in cells expressing KIF22-GFP T463D (median
631 $5.8 \mu\text{m}$) compared to cells expressing wild type KIF22-GFP ($12.5 \mu\text{m}$) or KIF22-GFP T463A (10.8
632 μm) (**Figure 8F**). As in cells expressing KIF22-GFP with pathogenic mutations, the severity of

633 anaphase chromosome recongression, indicated by the distance between chromosome masses
634 at 7 minutes, was dependent on GFP expression level (Spearman correlation coefficient -0.3964,
635 one-tailed p value 0.0004) (**Figure S5E**). When only cells expressing lower levels of KIF22-GFP
636 (mean background subtracted intensity <100 arbitrary units) were considered, the same effect
637 (expression of KIF22-GFP T463D causes recongression) was still observed (**Figure S5F, S5G**).
638 This recongression phenocopies the effect of pathogenic mutations on anaphase chromosome
639 segregation, consistent with pathogenic mutations preventing anaphase inactivation of KIF22.

640 In addition to causing the same defects in anaphase chromosome segregation, expression
641 of KIF22-GFP T463D also affects daughter cell nuclear morphology. Cells expressing KIF22-GFP
642 T463D have lobed and fragmented nuclei (**Figure S5H**) and correspondingly reduced nuclear
643 solidity measurements (**Figure 8G**). An increased percentage of cells expressing KIF22-GFP
644 T463D in the presence of endogenous KIF22 (65%) or in cells depleted of endogenous KIF22
645 (72%) have abnormally shaped nuclei, as indicated by a solidity value below the fifth percentile
646 of control cell nuclear solidity (**Figure 8H**).

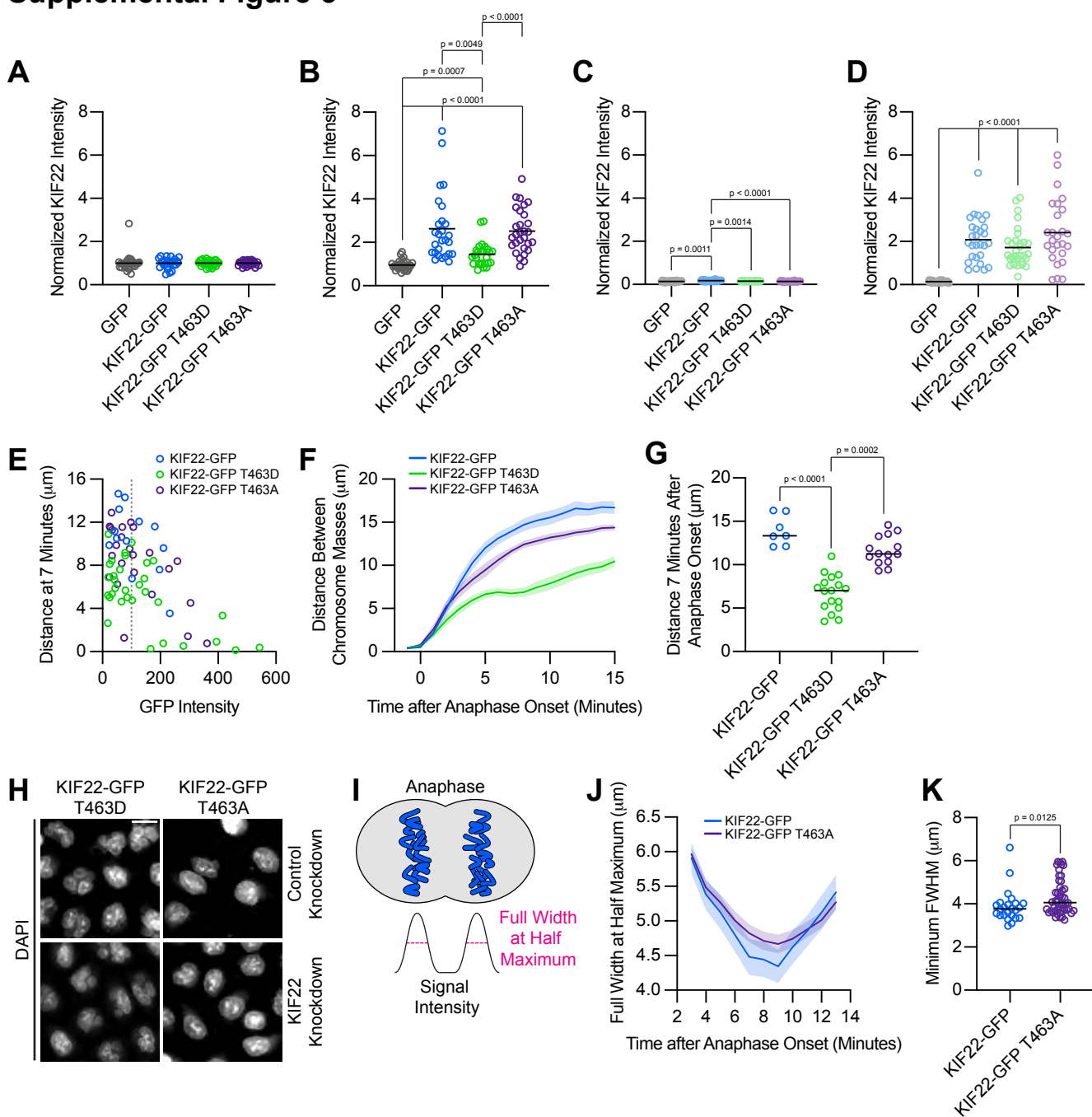
647 Expression of KIF22-GFP T463A also resulted in a small increase in the percentage of
648 abnormally shaped nuclei (26% in control or KIF22 knockdown conditions) (**Figure 8H**). Since
649 expression of KIF22-GFP T463A does not cause anaphase recongression (**Figure 8E**), the level
650 of compaction of the segregating chromosome masses was explored as a possible explanation
651 for this modest increase in the percentage of cells with nuclear morphology defects. In KIF22
652 knockout mice, loss of KIF22 reduces chromosome compaction in anaphase, causing the
653 formation of multinucleated cells (Ohsugi et al. 2008). The phosphonull T463A mutation reduces
654 KIF22 activity and may therefore exhibit a KIF22 loss of function phenotype. Measurement of the
655 widths of separating chromosome masses in anaphase (**Figure S5I**) did demonstrate a modest
656 broadening of the chromosome masses in cells expressing KIF22-GFP T463A (**Figure S5J,**
657 **S5K**), which may contribute to the modest defects in nuclear morphology seen in these cells.

Figure 8



658 **Figure 8: Phosphomimetic mutation of T463 phenocopies pathogenic mutations in KIF22.**
659 **(A)** Immunofluorescence images of monopolar HeLa-Kyoto cells. KIF22-GFP was visualized
660 using an anti-GFP antibody. Fixed approximately 2-3 hours after treatment with monastrol and 24
661 hours after siRNA transfection and treatment with doxycycline to induce expression. Scale bar 5
662 μm . Images are representative of 3 or more experiments. **(B)** Distance from the spindle pole to
663 the maximum DAPI signal, a measure of relative polar ejection force level, between HeLa-Kyoto
664 cell lines expressing KIF22-GFP with phosphomimetic and phosphonull mutations. 26-29 cells
665 from 3 experiments per condition. **(C)** Distance from the spindle pole to the maximum DAPI signal
666 in cells depleted of endogenous KIF22 and expressing KIF22-GFP with phosphomimetic and
667 phosphonull mutations. 27-47 cells from 3-4 experiments per condition. For B-C, bars indicate
668 means. p values from Brown-Forsythe and Welch ANOVA with Dunnett's T3 multiple comparisons
669 test. p values are greater than 0.05 for comparisons without a marked p value. **(D)** Time-lapse
670 images of dividing HeLa-Kyoto cells. Cells expressing KIF22-GFP T463D exhibit recongression
671 of the chromosomes during anaphase. Times indicate minutes after anaphase onset. Images are
672 maximum intensity projections in z through the entirety of the spindle. Imaged approximately 18
673 hours after treatment with doxycycline to induce expression. Scale bar 5 μm . Images are
674 representative of 3 or more experiments. **(E)** Distance between separating chromosome masses
675 throughout anaphase in HeLa-Kyoto cells. Lines represent the mean and the shaded area
676 denotes SEM. 13-32 cells from 5 experiments per condition. **(F)** Distance between separating
677 chromosome masses 7 minutes after anaphase onset. Bars indicate medians. p values from
678 Kruskal-Wallis test. p values are greater than 0.05 for comparisons without a marked p value. 13-
679 32 cells from 5 experiments per condition. **(G)** Measured solidity of nuclei in HeLa-Kyoto cell lines.
680 Small circles represent the solidity of individual nuclei, and large circles with black outlines
681 indicate the median of each experiment. A dashed line marks a solidity value of 0.950, the fifth
682 percentile of solidity for control cells transfected with control siRNA and expressing GFP. **(H)**
683 Percentage of nuclei with abnormal shape, indicated by a solidity value less than 0.950, the fifth
684 percentile of control (control knockdown, GFP expression) cell solidity. A chi-square test of all
685 data produced a p value < 0.0001 . Plotted p values are from pairwise post-hoc chi-square tests
686 comparing control (control knockdown, GFP expression) cells to each other condition. Applying
687 the Bonferroni correction for multiple comparisons, a p value of less than 0.00714 was considered
688 significant. p values are greater than 0.00714 for comparisons without a marked p value. Data in
689 (G) and (H) represent 312-376 cells from 3 experiments per condition.

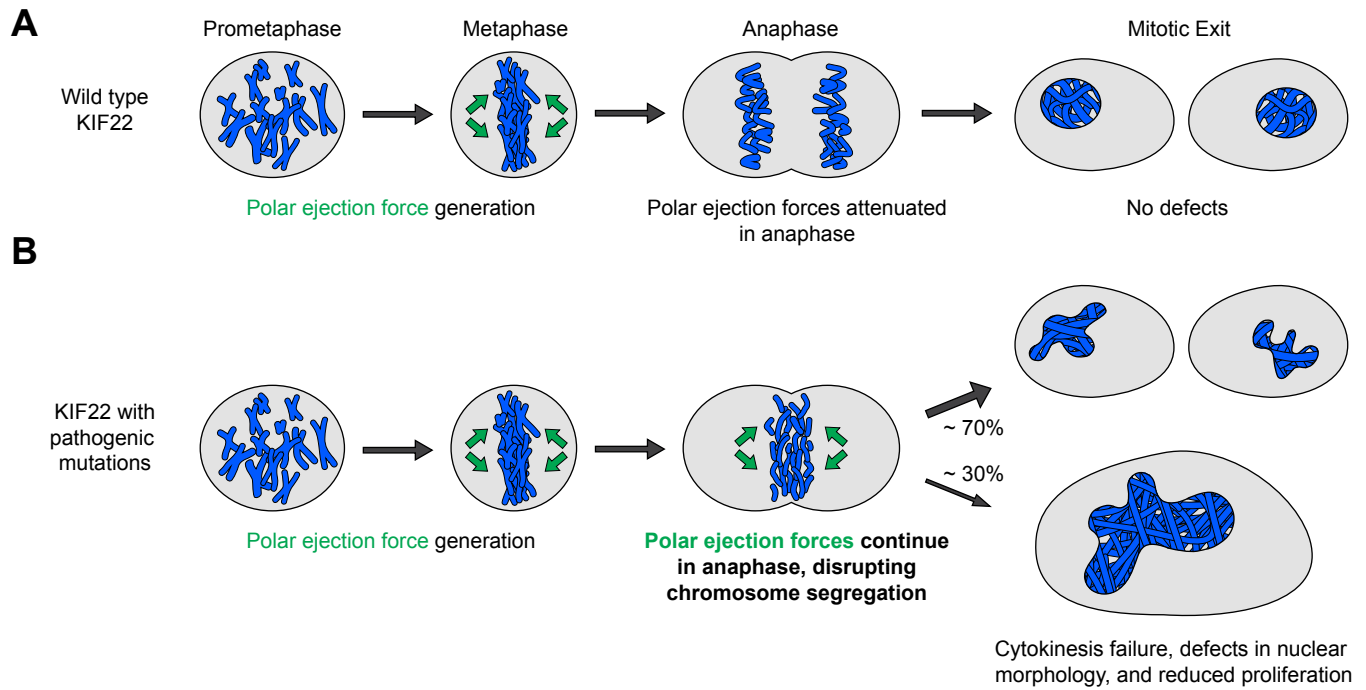
Supplemental Figure 5



690 **Supplemental Figure 5: Cells expressing KIF22-GFP T463A have broader anaphase**
691 **chromosome masses.**

692 **(A-D)** Quantification of KIF22 fluorescence intensity in untreated HeLa-Kyoto cells transfected
693 with control siRNA (A), cells treated with doxycycline to induce expression and transfected with
694 control siRNA (B), untreated cells transfected with KIF22 siRNA (C), and cells treated with
695 doxycycline and transfected with KIF22 siRNA (D) normalized to the mean intensity of uninduced,
696 control knockdown cells (endogenous KIF22 expression level) for each cell line (A). 23-32 HeLa-
697 Kyoto cells per condition from 3 experiments. **(E)** Plotting background-subtracted GFP intensity
698 against the distance between separating chromosome masses at 7 minutes indicates that this
699 distance is dependent on expression level (Spearman correlation coefficient -0.3964, one-tailed
700 p value = 0.0004). Grey dashed line indicates mean background subtracted GFP intensity of 100.
701 13-32 cells from 5 experiments per condition. **(F)** Distance between separating chromosome
702 masses of cells expressing lower levels of KIF22-GFP (mean background subtracted GFP
703 intensity less than 100). Lines represent the mean and the shaded area denotes SEM. 7-14 cells
704 from 4-5 experiments per condition. **(G)** Distance between separating chromosome masses 7
705 minutes after anaphase onset of cells expressing lower levels of KIF22-GFP (mean background
706 subtracted GFP intensity less than 100). Bars indicate medians. p values from Kruskal-Wallis test.
707 p values are greater than 0.05 for comparisons without a marked p value. 7-14 cells from 4-5
708 experiments per condition. **(H)** DAPI-stained nuclei of HeLa-Kyoto cells. Fixed approximately 24
709 hours after treatment with doxycycline to induce expression. Scale bar 20 μm . Images are
710 representative of 3 or more experiments. **(I)** Schematic depicting the measurement of
711 chromosome signal intensity in anaphase and the use of the full width at half maximum (FWHM)
712 as a measure of anaphase chromosome mass broadness. **(J)** Full width at half maximum of the
713 plotted intensities of separating chromosome masses of HeLa-Kyoto cells expressing KIF22-GFP
714 or KIF22-GFP T463A. Lines represent the mean and the shaded area denotes SEM. **(K)** Minimum
715 FWHM value, representing maximal anaphase chromosome compaction, between cells
716 expressing KIF22-GFP and KIF22-GFP T463A. p value from Mann-Whitney test. Bars represent
717 medians. Data in (J) and (K) represent 24-48 cells from 5 experiments per condition.

Figure 9



718 **Figure 9. Pathogenic mutations disrupt the anaphase, but not prometaphase, function of**
719 **KIF22.**

720 **(A)** Wild type KIF22 generates polar ejection forces to contribute to chromosome congression
721 and alignment in prometaphase. In anaphase, KIF22 inactivation results in the attenuation of polar
722 ejection forces (green arrows), allowing chromosomes to segregate toward the poles. Daughter
723 cells form regularly shaped nuclei and continue to proliferate. **(B)** In cells expressing KIF22 with
724 pathogenic (P148L, P148S, R149L, R149Q, V475G) or phosphomimetic (T463D) mutations,
725 prometaphase proceeds as in cells expressing wild type motor. Mutant KIF22 is capable of polar
726 ejection force generation. In anaphase, KIF22 fails to inactivate, resulting in continued generation
727 of polar ejection forces, which disrupts anaphase chromosome segregation. Daughter cells exhibit
728 nuclear morphology defects. In about 30% of cells, cytokinesis fails, and proliferation rates are
729 reduced.

730 **DISCUSSION**

731 We have determined that pathogenic mutations in KIF22 disrupt anaphase chromosome
732 segregation, causing chromosome recongression, nuclear morphology defects, reduced
733 proliferation, and, in a subset of cells, cytokinesis failure. Wild type KIF22 is inactivated in
734 anaphase (Soeda et al. 2016), resulting in an attenuation of polar ejection forces, which allows
735 chromosomes to move towards the spindle poles (**Figure 9A**). The phenotypes we observe in
736 cells expressing KIF22-GFP with pathogenic mutations are consistent with KIF22 remaining
737 active in anaphase (**Figure 9B**). Polar ejection forces could cause recongression by continuing
738 to push chromosomes away from the spindle poles during anaphase. These forces would result
739 in aberrant positioning of chromosomes during telophase and cytokinesis, which could cause the
740 nuclear morphology defects and cytokinesis failure we observe in cells expressing mutant KIF22-
741 GFP. Consistent with this model, mimicking phosphorylation of T463 to prevent KIF22 inactivation
742 in anaphase phenocopies the effects of pathogenic mutations. Thus, we conclude that pathogenic
743 mutations result in a gain of KIF22 function, which aligns with findings that KIF22 mutations are
744 dominant in heterozygous patients (Min et al. 2011; Boyden et al. 2011; Tüysüz et al. 2014). The
745 effects of pathogenic mutations on chromosome movements in anaphase are consistent with
746 observations of chromosome recongression in cells with altered CDK1 activity (Wolf et al. 2006;
747 Su et al. 2016) or altered tail structure (Soeda et al. 2016). Our work additionally demonstrates
748 the consequences of this recongression on cytokinesis, daughter cell nuclear morphology, and
749 proliferation.

750 Mutations in both the motor domain (P148L, P148S, R149L, and R149Q) and the coiled-
751 coil domain (V475G) of KIF22 disrupt chromosome segregation in a manner consistent with a
752 failure of KIF22 inactivation in anaphase. This finding could contribute to our understanding of the
753 mechanism by which KIF22 is inactivated, adding to studies that demonstrate that deletion of the
754 tail microtubule binding domain and deletion or disruption of the coiled-coil domain also prevents
755 the inactivation of KIF22 in anaphase (Soeda et al. 2016). Given that mutations in the tail and
756 motor domain of KIF22 both disrupt chromosome segregation, the tail and motor domain may
757 interact to inactivate the motor. Head-tail autoinhibition is a known regulatory mechanism of other
758 members of the kinesin superfamily (Verhey et al. 1998; Coy et al. 1999; Friedman and Vale
759 1999; Imanishi et al. 2006; Espeut et al. 2008; Hammond et al. 2009; Hammond et al. 2010; Ren
760 et al. 2018; Blasius et al. 2021; Verhey and Hammond 2009), and disruption of autoinhibition can
761 be a mechanism of disease pathogenesis (van der Vaart et al. 2013; Cheng et al. 2014; Bianchi
762 et al. 2016; Asselin et al. 2020; Blasius et al. 2021). Mutations in either the tail or motor domain
763 could disrupt this interaction, preventing KIF22 inactivation in anaphase. As amino acids P148,

764 R149, and V475 are highly conserved across species in members of the kinesin-10 family (**Figure**
765 **1C**), this inactivation mechanism may be present in these motors as well.

766 Alternatively, it has been proposed that the tail of KIF22 may interact with microtubules to
767 suspend polar ejection force generation (Soeda et al. 2016). In this framework, the mutation in
768 the tail of KIF22 (V745G) could disrupt anaphase chromosome segregation by altering this
769 interaction with microtubules. Motor domain mutations would not be expected to alter the
770 interaction of the tail with the surface of microtubules, and in this model would cause the same
771 cellular phenotype by altering KIF22 inactivation via a different mechanism, potentially related to
772 the mechanochemical cycle of the motor given the location of these mutations in the $\alpha 2$ helix. An
773 additional alternative model for how pathogenic mutations affect the inactivation of KIF22 in
774 anaphase could be that mutations alter phosphoregulation of KIF22 activity. If mutations
775 prevented the dephosphorylation of T463 in anaphase this could cause anaphase recongression.
776 However, addition of a phosphonull T463A mutation to KIF22 with coiled-coil or microtubule
777 binding domain deletions does not rescue anaphase chromosome recongression defects (Soeda
778 et al. 2016), suggesting that the role of the KIF22 tail in motor inactivation is not only to facilitate
779 dephosphorylation of T463.

780 While chromosomes in some cells, particularly those expressing KIF22-GFP at high
781 levels, completely failed to segregate and decondensed in the center of the spindle, most cells
782 demonstrated chromosome recongression wherein poleward motion of chromosomes begins, but
783 then chromosomes switch direction and move anti-poleward. These dynamics may be due to
784 differences in microtubule density closer to the poles compared to the center of the spindle. This
785 model is consistent with work demonstrating that in monopolar spindles, poleward movement of
786 chromosomes is limited by chromosomes reaching a threshold density of microtubules at which
787 polar ejection forces are sufficient to cause chromosomes to switch to anti-poleward movement
788 (Cassimeris et al. 1994). We observed that chromosomes on the periphery of the spindle remain
789 closer to the poles while central chromosomes are pushed further away from the poles during
790 recongression in cells expressing KIF22-GFP with pathogenic mutations. This could also be
791 explained by the central chromosomes encountering a higher density of microtubules, and KIF22
792 bound to these chromosomes therefore generating higher levels of polar ejection forces. In
793 addition, this mechanism is consistent with observations that oscillations of peripheral
794 chromosomes are reduced compared to chromosomes at the center of the spindle (Cimini et al.
795 2004; Cameron et al. 2006; Stumpff et al. 2008; Civelekoglu-Scholey et al. 2013), which could

796 also be explained by reduced peripheral microtubule density limiting peripheral polar ejection
797 force generation.

798 Our assessment of the relative trajectories of chromosomes, centromeres, and spindle
799 poles offers insight into the relative magnitudes of polar ejection forces and other anaphase
800 forces. Expression of KIF22-GFP with pathogenic mutations did not alter the distance between
801 centromeres and spindle poles, indicating that while anaphase polar ejection forces altered the
802 position of chromosome arms within the spindle, these forces were not sufficient to prevent the
803 shortening of k-fibers. However, the expression of mutant KIF22-GFP does also alter the
804 movements of the spindle poles, allowing assessment of the relative magnitude of polar ejection
805 forces compared to the forces generated by the sliding of antiparallel spindle microtubules to
806 separate the spindle poles in anaphase (Sawin et al. 1992; Nislow et al. 1992; Straight et al. 1998;
807 Brust-Mascher et al. 2004; Tanenbaum et al. 2009; Fu et al. 2009; van Heesbeen et al. 2014;
808 Vukušić et al. 2021; Vukušić et al. 2019). In cells expressing mutant KIF22-GFP, spindle pole
809 separation stalled, and poles moved closer to one another during anaphase chromosome
810 recondensation. This suggests that the polar ejection forces collectively generated by mutant KIF22
811 motors are of greater magnitude than the forces sliding the spindle poles apart during anaphase
812 B. Although it is important to note that this phenotype was observed with moderate
813 overexpression of mutant KIF22, the observed effects on spindle pole separation underscore the
814 importance of KIF22 inactivation, and imply that reducing polar ejection forces is required for both
815 anaphase A and anaphase B. This force balance may differ between cell types, as tail domain
816 deletions that alter chromosome movements do not disrupt anaphase B in mouse oocyte meiosis
817 (Soeda et al. 2016).

818 Patients with mutations in KIF22 exhibit defects in skeletal development. The pathology
819 observed in the patient heterozygous for the V475G mutation differs from those seen in SEMDYL2
820 patients with motor domain mutations (**Figure 1E, 1F**) (Min et al. 2011; Boyden et al. 2011; Tüysüz
821 et al. 2014). However, a meaningful comparison of pathologies between patients is limited both
822 by the fact that only a single patient with a mutation in the tail of KIF22 has been identified, and
823 by the considerable variation in clinical presentation between patients with motor domain
824 mutations, even between patients with the same point mutation (Min et al. 2011; Boyden et al.
825 2011; Tüysüz et al. 2014). The defects in chromosome segregation we observed in cells
826 expressing mutant KIF22-GFP may contribute to skeletal developmental pathogenesis. Mutations
827 could cause reduced proliferation of growth plate chondrocytes, which in turn could limit bone
828 growth. Disrupting cytokinesis in the growth plate causes shorter bones and stature in mice (Gan
829 et al. 2019), and mutations in KIF22 could affect development via this mechanism. The presence

830 of pathologies in other cartilaginous tissues, including the larynx and trachea, in patients with
831 mutations in the motor domain of KIF22 (Boyden et al. 2011) is also consistent with a disease
832 etiology based in aberrant chondrocyte proliferation. Defects in mitosis could result in tissue-
833 specific patient pathology based on differences in force balance within anaphase spindles in
834 different cell types arising from different expression or activity levels of mitotic force generators or
835 regulators. Growth plate chondrocytes, particularly, are organized into columns and must divide
836 under geometric constraints (Dodds 1930), which could increase sensitivity to anaphase force
837 imbalances. Additionally, we cannot exclude the possibility that these mutations may affect the
838 function of interphase cells, which could affect development via a mechanism independent from
839 the effects of the mutations on mitosis. Future work will be required to distinguish among these
840 possible explanations.

841

842 **MATERIALS AND METHODS**

843 **Patient assessment**

844 Clinical exome sequencing was performed by the Department of Laboratory Medicine and
845 Pathology at Mayo Clinic in Rochester, Minnesota, USA as previously described (Cousin et al.
846 2019). Carbohydrate deficient transferrin testing for congenital disorders of glycosylation was
847 performed at Mayo Clinic Laboratories, Rochester, Minnesota, USA (Lefeber et al. 2011).

848

849 **Cell culture**

850 HeLa-Kyoto and RPE-1 cell lines were grown in Minimum Essential Media α (Gibco
851 #12561-056) supplemented with 10% fetal bovine serum (Gibco #16000-044) at 37°C with 5%
852 CO₂. Cell lines were validated by short tandem repeat (STR) DNA typing using the Promega
853 GenePrint 10 System according to the manufacturer's instructions (Promega #B9510). Cells were
854 cryopreserved in Recovery Cell Culture Freezing Medium (Gibco #12648-010). HeLa-Kyoto and
855 RPE-1 acceptor cell lines for recombination (both gifts from Ryoma Ohi, University of Michigan)
856 were maintained in media supplemented with 10 μ g/mL blasticidin (Thermo Fisher Scientific
857 #R21001).

858

859 **Transfection**

860 siRNA transfection was performed using Lipofectamine RNAiMax Transfection Reagent
861 (Thermo Fisher Scientific #13778150) in Opti-MEM Reduced Serum Media (Gibco #31985-062).
862 KIF22 was targeted for siRNA-mediated depletion using a Silencer Validated siRNA (Ambion
863 #AM51331, sense sequence GCUGCUCUCUAGAGAUUGCTT). Control cells were transfected

864 with Silencer Negative Control siRNA #2 (Ambion #AM4613). DNA transfections were performed
865 using Lipofectamine LTX (Thermo Fisher Scientific #15338100) in Opti-MEM Reduced Serum
866 Media (Gibco #31985-062).

867

868 **Plasmids**

869 Plasmids related to the generation of inducible cell lines are described in Table 1. A C-
870 terminally tagged KIF22-GFP plasmid was constructed by adding EcoRI and KpnI sites to the
871 KIF22 open reading frame (from pJS2161 (Stumpff et al. 2012)), performing a restriction digest,
872 and ligating the products into a digested pEGFP-N2 vector (Clontech) (pAT4206). Site-directed
873 mutagenesis was performed to add silent mutations for siRNA resistance (pAT4226). The open
874 reading frame from pAT4226 and the pEM791 vector (Khandelia et al. 2011) were amplified and
875 combined using Gibson Assembly (New England BioLabs) to generate a plasmid for
876 recombination-mediated construction of inducible cell lines (pAT4250). Site-directed mutagenesis
877 was performed on pAT4250 to generate plasmids encoding KIF22-GFP P148L, P148S, R149L,
878 R149Q, V475G, T463D, and T463A for recombination. See Table 1 for primer sequences.

879 The mCh-CAAX plasmid was a gift from Alan Howe (University of Vermont). The mCh-
880 NLS plasmid was generated by Michael Davidson and obtained from Addgene (mCh-Nucleus-7,
881 #55110). The pericentrin-RFP plasmid (Gillingham and Munro 2000) was a gift from Sean Munro
882 (MRC Laboratory of Molecular Biology). The CENPB-mCh plasmid (D. Liu et al. 2010) was
883 generated by Michael Lampson and obtained from Addgene (#45219).

884

885 **Generation of inducible cell lines**

886 Inducible cell lines were generated using recombination-mediated cassette exchange as
887 previously described (Khandelia et al. 2011). Briefly, plasmids (see Table 1) encoding siRNA-
888 resistant KIF22-GFP constructs were cotransfected with a plasmid encoding nuclear localized
889 Cre recombinase (pEM784) into HeLa-Kyoto (Sturgill et al. 2016) or RPE-1 acceptor cells using
890 Lipofectamine LTX transfection (Thermo Fisher Scientific #15338100). For HeLa-Kyoto cell lines,
891 24 hours after transfection cells were treated with 1 $\mu\text{g}/\text{mL}$ puromycin (Thermo Fisher Scientific
892 #A11139-03) for 48 hours, then 2 $\mu\text{g}/\text{mL}$ puromycin for 48 hours for more stringent selection, and
893 finally 1 $\mu\text{g}/\text{mL}$ puromycin until puromycin-sensitive cells were eliminated. Selection of RPE-1
894 cells was accomplished via treatment with 5 $\mu\text{g}/\text{mL}$ puromycin for 48 hours beginning 24 hours
895 after transfection, then 10 $\mu\text{g}/\text{mL}$ puromycin for 48 hours, and finally 5 $\mu\text{g}/\text{mL}$ puromycin until
896 puromycin-sensitive cells were eliminated. Inducible cell lines were maintained in puromycin
897 (HeLa-Kyoto 1 $\mu\text{g}/\text{mL}$, RPE-1 5 $\mu\text{g}/\text{mL}$) for continued selection. To confirm the sequence of

898 inserted DNA in the selected cell populations, genomic DNA was extracted using the QIAmp DNA
899 Blood Mini Kit (Qiagen #51106) and subjected to sequencing (Eurofins). Expression of inserted
900 DNA sequences was induced via treatment with 2 μ g/mL doxycycline (Thermo Fisher Scientific
901 #BP26531).

902

903 **Immunofluorescence**

904 For fixed cell imaging, cells were grown on 12 mm glass coverslips in 24-well plates. Cells
905 were fixed in 1% paraformaldehyde in ice-cold methanol for 10 minutes on ice. Cells were blocked
906 for 1 hour using 20% goat serum (Gibco #16210-064) in antibody dilution buffer (AbDil, 1% bovine
907 serum albumin (Sigma Aldrich #B4287), 0.1% Triton X-100 (Sigma Aldrich #93443), 0.02%
908 sodium azide (Fisher Scientific #BP9221) in TBS) and incubated with the following primary
909 antibodies for one hour at room temperature: mouse anti- α -tubulin (DM1 α) 1:500 (Millipore Sigma
910 #T6199), rat anti-tubulin clone YL1/2 1:1500 (Millipore Sigma #MAB1864), rabbit anti-KIF22 1:500
911 (GeneTex #GTX112357), mouse anti-centrin 1:500 (Millipore Sigma #04-1624), or rabbit anti-
912 GFP 1:1000 (Invitrogen #A11121). Cells were incubated with secondary antibodies conjugated to
913 AlexaFluor 488, 594, or 647 (Invitrogen Molecular Probes #A11034, A11037, A21245, A11029,
914 A11032, A21236, A11007) for one hour at room temperature. Coverslips were mounted on slides
915 using Prolong Gold mounting medium with DAPI (Invitrogen Molecular Probes #P36935).

916

917 **Microscopy**

918 Images were acquired using a Nikon Ti-E or Ti-2E inverted microscope driven by NIS
919 Elements software (Nikon Instruments). Images were captured using a Clara cooled charge-
920 coupled device (CCD) camera (Andor) or Prime BSI scientific complementary metal-oxide-
921 semiconductor (sCMOS) camera (Teledyne Photometrics) with a Spectra-X light engine
922 (Lumencore). Samples were imaged using Nikon objectives Plan Apo 40X 0.95 numerical
923 aperture (NA), Plan Apo λ 60X 1.42 NA, and APO 100X 1.49 NA. For live imaging, cells were
924 imaged in CO₂-independent media (Gibco #18045-088) supplemented with 10% fetal bovine
925 serum (Gibco #16000-044) in a 37° C environmental chamber. Images were processed and
926 analyzed using Image J/FIJI (Schneider et al. 2012; Schindelin et al. 2012).

927

928 **KIF22-GFP expression level quantitation**

929 HeLa-Kyoto or RPE-1 cells were treated with 2 μ g/mL doxycycline to induce expression
930 and transfected with control or KIF22 siRNA approximately 24 hours prior to fixation. Metaphase
931 cells were imaged for measurement of KIF22 expression levels. Measurements of KIF22

932 immunofluorescence intensity were made in a background region of interest (ROI) containing no
933 cells and an ROI representing the chromosomes, identified by thresholding DAPI signal. The
934 mean background subtracted KIF22 signal on the chromosomes was calculated by subtracting
935 the product of the mean background intensity and the chromosome ROI area from the
936 chromosome ROI integrated density and dividing by the area of the chromosome ROI. KIF22
937 intensities were normalized to the mean KIF22 intensity in control cells (control knockdown,
938 uninduced) in each experimental replicate.

939

940 **Metaphase chromosome spreads**

941 RPE-1 cells were grown in 60 mm dishes for approximately 24 hours. Media was
942 exchanged to fresh growth media for 2 hours to promote mitosis. Cells were arrested in 0.02
943 $\mu\text{g}/\text{mL}$ colcemid (Gibco KaryoMAX #15212012) for three hours at 37°C, then trypsinized, pelleted,
944 and gently re-suspended in 500 μL media. 5 mL 0.56% KCl hypotonic solution was added
945 dropwise to the cell suspension, which was then incubated for 15 minutes in a 37°C water bath.
946 Cells were pelleted, gently resuspended, and fixed via the addition of 1 mL ice-cold 3:1
947 methanol:glacial acetic acid. Cells were pelleted and resuspended in fixative an additional three
948 times, then stored at -20°C. Metaphase chromosome spreads were prepared by humidifying the
949 surface of glass slides by exposing them to the steam above a 50°C water bath, placing the slides
950 at an angle relative to the work surface, and dropping approximately 100 μL of ice-cold cell
951 suspension onto the slide from a height of approximately one foot. Slides were dried on a hot
952 plate, then covered with Prolong Gold mounting medium with DAPI (Invitrogen Molecular Probes
953 #P36935) and sealed.

954

955 **Fluorescence recovery after photobleaching**

956 HeLa-Kyoto cells were seeded in glass-bottom 35 mm dishes (Greiner Bio-One #627975
957 and #627965) and treated with 2 $\mu\text{g}/\text{mL}$ doxycycline to induce expression 18-24 hours before
958 imaging. Cells were imaged at 5 second intervals for 25 seconds before bleaching, photobleached
959 using a point-focused 405 nm laser, and imaged at 20 second intervals for 10 minutes after
960 bleaching. Fluorescence intensities in bleached, unbleached, and background regions of each
961 frame were measured using a circular ROI, area 0.865 μm^2 . For interphase and metaphase cells,
962 unbleached measurements were made on the opposite side of the nucleus or chromosome mass
963 as the bleached measurements. For anaphase cells, one segregating chromosome mass was
964 bleached, and unbleached measurements were made on the opposite chromosome mass.

965 Background intensities, measured in cell-free area, were subtracted from bleached and
966 unbleached intensities. Background-subtracted intensities were normalized to the intensity of the
967 first frame imaged.

968

969 **Polar ejection force assay**

970 HeLa-Kyoto cells were treated with 2 $\mu\text{g}/\text{mL}$ doxycycline to induce expression and
971 transfected with control or KIF22 siRNA approximately 24 hours prior to fixation. Cells were
972 arrested in 100 μM monastrol (Selleckchem #S8439) for 2-3 hours before fixation. Monopolar
973 mitotic cells oriented perpendicular to the coverslip were imaged at the focal plane of the spindle
974 pole for polar ejection force measurements. A circular ROI with a 12.5 μm radius was centered
975 around the spindle pole of each cell, and the radial profile of DAPI signal intensity at distances
976 from the pole was measured (Radial Profile Plot plugin, <https://imagej.nih.gov/ij/plugins/radial-profile.html>). The distance from the pole to the maximum DAPI signal was calculated for each cell
977 as a measure of relative polar ejection forces.
978

979

980 **Analyses of anaphase chromosome segregation**

981 HeLa-Kyoto or RPE-1 cells were treated with 2 $\mu\text{g}/\text{mL}$ doxycycline to induce expression
982 approximately 18 hours before imaging. For HeLa-Kyoto cells, media was exchanged to CO_2 -
983 independent media containing 2 $\mu\text{g}/\text{mL}$ doxycycline and 100 nM SiR-Tubulin (Spirochrome
984 #SC002) approximately 1-1.5 hours before imaging. For RPE-1 cells, media was exchanged to
985 CO_2 -independent media containing 2 $\mu\text{g}/\text{mL}$ doxycycline, 20-100 nM SiR-Tubulin (Spirochrome
986 #SC002), and 10 μM verapamil (Spirochrome #SCV01) approximately 1.5-3 hours before
987 imaging. Cells were imaged at 1 minute time intervals. Distances between segregating
988 chromosome masses were measured by plotting the KIF22-GFP signal intensity along a line
989 drawn through both spindle poles (macro available at <https://github.com/StumpffLab/Image-Analysis>). This data set was split at the center distance to generate two plots, each representing
990 one half-spindle/segregating chromosome mass. The distance between the maximum of each
991 intensity plot was calculated using MATLAB (Mathworks, Version R2018a) (script available at
992 <https://github.com/StumpffLab/Image-Analysis>). To assess the broadness of segregating
993 chromosome masses in cells expressing KIF22-GFP T463A, a Gaussian curve was fit to the same
994 intensity plots and the full width at half maximum was calculated in MATLAB.
995

996 To measure the movements of spindle poles and kinetochores in anaphase, HeLa-Kyoto
997 cells were seeded in glass-bottom 24-well plates (Cellvis #P24-1.5H-N) and cotransfected with
998 PCM-RFP and mCh-CENPB using Lipofectamine LTX (Thermo Fisher Scientific #15338100)

999 approximately 24 hours before imaging. Cells were treated with 2 $\mu\text{g}/\text{mL}$ doxycycline to induce
1000 expression approximately 12-18 hours before imaging. Cells were imaged at 20 second time
1001 intervals. To more clearly visualize spindle poles and kinetochores, images of PCM-RFP and
1002 mCh-CENPB signal were background subtracted by duplicating each frame, applying a gaussian
1003 blur (sigma 30 pixels), and subtracting this blurred image from the original. For each frame, a line
1004 was drawn between spindle poles (PCM-RFP signal) to measure the distance between them, and
1005 the intensity of KIF22-GFP and mCh-CENPB along this line was plotted. These data sets were
1006 split at the center distance to generate two plots, and the distance between plot maxima and the
1007 distance from maxima to the spindle poles were calculated using MATLAB (scripts available at
1008 <https://github.com/StumpffLab/Image-Analysis>).

1009

1010 **Assessment of cytokinesis failure**

1011 To visualize cell boundaries, HeLa-Kyoto cells were transfected with mCh-CAAX using
1012 Lipofectamine LTX approximately 24-32 hours before imaging and treated with 2 $\mu\text{g}/\text{mL}$
1013 doxycycline approximately 8 hours before imaging. Cells were imaged at 3-minute intervals. Cells
1014 were scored as failing cytokinesis if the product of mitosis was a single cell with a single boundary
1015 of mCh-CAAX signal.

1016

1017 **Nuclear morphology quantification**

1018 HeLa-Kyoto or RPE-1 cells were treated with 2 $\mu\text{g}/\text{mL}$ doxycycline to induce expression
1019 approximately 24 hours before fixation. Nuclear solidity was measured for each interphase
1020 nucleus in each imaged field. The 5th percentile of solidity for control cells (transfected with control
1021 siRNA and expressing GFP) was used as a threshold below which nuclear solidity was considered
1022 abnormal.

1023 To assess the ability of nuclei to retain nuclear-localized proteins, cells were transfected
1024 with mCh-NLS using Lipofectamine LTX approximately 24-32 hours before imaging and treated
1025 with 2 $\mu\text{g}/\text{mL}$ doxycycline approximately 8 hours before imaging. Cells were imaged at 3-minute
1026 intervals during and after division, and the presence of mCh-NLS signal in all nuclear structures
1027 (KIF22-GFP positive regions) was assessed.

1028

1029 **Assessment of spindle dependence of nuclear morphology defects**

1030 To assess whether nuclear morphology defects caused by KIF22 depend on force
1031 generation within the mitotic spindle, cells were treated with 2 $\mu\text{g}/\text{mL}$ doxycycline approximately
1032 8 hours before imaging, SPY595-DNA (1X per manufacturer's instructions) (Spirochrome

1033 #SC301) approximately 1.5-2 hours before imaging, and 500 nM nocodazole (Selleckchem
1034 #S2775) and 900 nM reversine (Cayman Chemical #10004412) approximately 0.5-1 hour before
1035 imaging. Cells were imaged at 5-minute intervals. Nuclear solidity was measured 15 minutes
1036 before chromosome condensation and 100 minutes after chromosome decondensation.

1037

1038 **Proliferation assay**

1039 HeLa-Kyoto cells were seeded in a 96-well plate and treated with 2 $\mu\text{g}/\text{mL}$ doxycycline to
1040 induce expression or transfected with KIF22 siRNA approximately eight hours before the first
1041 assay timepoint. Automated bright field imaging using a Cytation 5 Cell Imaging Multi-Mode
1042 Reader (Biotek) (4X Plan Fluorite 0.13 NA objective (Olympus)) driven by Gen5 software (Biotek)
1043 was used to measure cell proliferation (Marquis et al. 2021). Images were collected every 4 hours
1044 for 96 hours. Gen5 software was used to process images and count the number of cells in each
1045 imaged field. Cell counts were normalized to the cell count in the first image acquired at time 0.
1046 Fold change at 96 hours was calculated by dividing the cell count at 96 hours by the cell count at
1047 time 0. Predicted cell counts at 48 hours were calculated using an experimentally determined
1048 doubling time of 20.72 hours for the control case where all cells divide ($Cells_T = 2^{\left(\frac{T}{20.72}\right)}$), the case
1049 where nuclear morphology defects limit proliferation and 60% of cells do not divide ($Cells_T =$
1050 $1.4^{\left(\frac{T}{20.72}\right)}$), and the case where cytokinesis failure limits proliferation and 30% of cells do not divide
1051 ($Cells_T = 1.7^{\left(\frac{T}{20.72}\right)}$).

1052

1053 **Statistical analyses**

1054 Statistical tests were performed using GraphPad Prism software (GraphPad Software,
1055 Inc.), version 9.2.0. Specific statistical tests and n values for reported data are indicated in the
1056 figure legends. All data represent a minimum of three independent experiments.

1057 **Table 1**

Plasmid	Description	Primers (5' to 3', Fw: Forward, Rev: Reverse)	Source
pEM784	nlCre recombinase	NA	Khandelia 2011 PMID 21768390
pEM791	EGFP for recombination	NA	Khandelia 2011 PMID 21768390
pJS2161	GFP-KIF22	NA	Stumpff 2012 PMID 22595673
pAT4206	KIF22-GFP	Fw: TACGTGGAATTCCACCATGGCCGCGGGCGGCTCGA Rev: GTGACTGGTACCTGGAGGCGCCACAGCGCTGGC	This study
pAT4226	KIF22-GFP, siRNA resistant	Fw: GGGCATGGACAGCTGCTCACTCGAAATCGCTAACTGGAGGA ACCAC Rev: GTGGTTCCTCCAGTTAGCGATTTTCGAGTGAGCAGCTGTCCA TGCC	This study
pAT4250	KIF22-GFP, siRNA resistant, for recombination	Fragment Fw: CTGGGCACCACCATGGCCGCG Fragment Rev: GCTAGCTCGATTACTTGTACAGCTCGTCCATGCC Vector Fw: GTACAAGTAATCGAGCTAGCATATGGATCCATATAACT Vector Rev: CATGGTGGTGCCAGTGCCTCACGACC	This study
pAT4251	KIF22-GFP R149Q, siRNA resistant, for recombination	Fw: GGGGTGATCCCGCAGGCTCTCATGGAC Rev: GTCCATGAGAGCCTGCGGGATCACCC	This study
pAT4258	KIF22-GFP V475G, siRNA resistant, for recombination	Fw: TGCTAATGAAGACAGGAGAAGAGAAGGACCT Rev: AGGTCCTTCTCTTCTCCTGTCTTCATTAGCA	This study
pAT4260	KIF22-GFP T463D, siRNA resistant, for recombination	Fw: CCCCTCTGTTGAGTGACCCAAAGCGAGAGC Rev: GCTCTCGCTTTGGGTCACTCAACAGAGGGG	This study
pAT4261	KIF22-GFP T463A, siRNA resistant, for recombination	Fw: CCTCTGTTGAGTGCCCCAAAGCGAG Rev: CTCGCTTTGGGGCACTCAACAGAGG	This study
pAT4264	KIF22-GFP R149L, siRNA resistant, for recombination	Fw: GGGTGATCCCGCTGGCTCTCATGGAC Rev: GTCCATGAGAGCCAGCGGGATCACCC	This study
pAT4269	KIF22-GFP P148L, siRNA resistant, for recombination	Fw: CCTGGGGTGATCCTGCGGGCTCTCATG Rev: CATGAGAGCCCGCAGGATCACCCAGG	This study
pAT4270	KIF22-GFP P148S, siRNA resistant, for recombination	Fw: CTGGGGTGATCTCGCGGGCTCTCATG Rev: CATGAGAGCCCGCAGGATCACCCAG	This study

1058 **ACKNOWLEDGEMENTS**

1059 This work was supported by NIH F31AR074887 to AFT and NIH R01GM121491 to JKS.
1060 We thank the Mayo Clinic Center for Individualized Medicine (CIM) for supporting this research
1061 through the CIM Investigative and Functional Genomics program. We thank Alan Howe for the
1062 mCh-CAAX plasmid, and Ryoma Ohi for reagents and acceptor cells for recombination-mediated
1063 cassette exchange. We thank Rachel Stadler for technical assistance with data analysis and
1064 thank Laura Reinholdt and Matthew Warman for constructive discussions regarding this work.
1065 The authors declare no competing financial interests.

1066

1067 **VIDEO LEGENDS**

1068 **Video 1. Fluorescence recovery after photobleaching of KIF22-GFP.**

1069 Fluorescence recovery after photobleaching (FRAP) in HeLa-Kyoto cells expressing KIF22-GFP
1070 (top), KIF22-GFP R149Q (middle), or KIF22-GFP V475G (bottom). Cells represent interphase
1071 (left), metaphase (middle), or anaphase (right). Bleaching occurred at time zero. Scale bar 10 μm .
1072 Cells were imaged at 5 second intervals for 25 seconds before bleaching, photobleached, and
1073 imaged at 20 second intervals for 10 minutes after bleaching. Playback at 10 frames per second.

1074

1075 **Video 2. Anaphase in HeLa-Kyoto cells.**

1076 Anaphase chromosome segregation in HeLa-Kyoto cells expressing KIF22-GFP (left), KIF22-
1077 GFP R149Q (middle), or KIF22-GFP V475G (right). Magenta: SiR-Tubulin, green: KIF22-GFP.
1078 Times indicate minutes after anaphase onset. Scale bar 5 μm . Cells were imaged at 1 minute
1079 intervals. Playback at 10 frames per second (600X real time).

1080

1081 **Video 3. Anaphase in RPE-1 cells.**

1082 Anaphase chromosome segregation in RPE-1 cells expressing KIF22-GFP (left), KIF22-GFP
1083 R149Q (middle), or KIF22-GFP V475G (right). Magenta: SiR-Tubulin, green: KIF22-GFP. Times
1084 indicate minutes after anaphase onset. Scale bar 5 μm . Cells were imaged at 1 minute intervals.
1085 Playback at 10 frames per second (600X real time).

1086

1087 **Video 4. Anaphase spindle pole separation.**

1088 Anaphase in HeLa-Kyoto cells expressing pericentrin-RFP (magenta), CENPB-mCh (magenta),
1089 and KIF22-GFP (cyan). Times indicate seconds after anaphase onset. Scale bar 5 μm . Cells were
1090 imaged at 20 second intervals. Playback at 15 frames per second (300X real time).

1091

1092 **Video 5. Cytokinesis and cytokinesis failure.**

1093 Mitosis and cytokinesis in HeLa-Kyoto cells expressing KIF22-GFP (left), KIF22-GFP R149Q
1094 (middle), or KIF22-GFP V475G (right) (all KIF22-GFP represented in green) and mCh-CAAX
1095 (magenta). Scale bar 10 μ m. Cells were imaged at 3 minute intervals. Playback at 25 frames per
1096 second (4500X real time).

1097

1098 **REFERENCES**

1099 Adzhubei, I.A. et al., 2010. A method and server for predicting damaging missense mutations.
1100 *Nature Methods*, 7(4), pp.248–249.

1101 Antonio, C. et al., 2000. Xkid, a chromokinesin required for chromosome alignment on the
1102 metaphase plate. *Cell*, 102(4), pp.425–435.

1103 Asbury, C.L., 2017. Anaphase A: Disassembling Microtubules Move Chromosomes toward
1104 Spindle Poles. *Biology*, 6(1), p.15.

1105 Asselin, L. et al., 2020. Mutations in the KIF21B kinesin gene cause neurodevelopmental
1106 disorders through imbalanced canonical motor activity. *Nature communications*, pp.1–18.

1107 Bianchi, S. et al., 2016. Structural basis for misregulation of kinesin KIF21A autoinhibition by
1108 CFEOM1 disease mutations. *Scientific Reports*, 6(1), pp.30668–16.

1109 Bieling, P., Kronja, I. and Surrey, T., 2010. Microtubule Motility on Reconstituted Meiotic
1110 Chromatin. *Current Biology*, 20(8), pp.763–769.

1111 Blasius, T.L. et al., 2021. Sequences in the stalk domain regulate auto-inhibition and ciliary tip
1112 localization of the immotile kinesin-4 KIF7. *Journal of cell science*, 134(13).

1113 Bodnar, A.G. et al., 1998. Extension of life-span by introduction of telomerase into normal
1114 human cells. *Science (New York, N.Y.)*, 279(5349), pp.349–352.

1115 Boyden, E.D. et al., 2011. Recurrent dominant mutations affecting two adjacent residues in the
1116 motor domain of the monomeric kinesin KIF22 result in skeletal dysplasia and joint laxity.
1117 *American journal of human genetics*, 89(6), pp.767–772.

1118 Brouhard, G.J. and Hunt, A.J., 2005. Microtubule movements on the arms of mitotic
1119 chromosomes: polar ejection forces quantified in vitro. *Proceedings of the National
1120 Academy of Sciences*, 102(39), pp.13903–13908.

1121 Brust-Mascher, I. et al., 2004. Model for anaphase B: role of three mitotic motors in a switch
1122 from poleward flux to spindle elongation. *Proceedings of the National Academy of Sciences*,
1123 101(45), pp.15938–15943.

1124 Cameron, L.A. et al., 2006. Kinesin 5-independent poleward flux of kinetochore microtubules in
1125 PtK1 cells. *The Journal of Cell Biology*, 173(2), pp.173–179.

- 1126 Cassimeris, L., Rieder, C.L. and Salmon, E.D., 1994. Microtubule Assembly and Kinetochores
1127 Directional Instability in Vertebrate Monopolar Spindles - Implications for the Mechanism of
1128 Chromosome Congression. *Journal of cell science*, 107, pp.285–297.
- 1129 Cheng, L. et al., 2014. Human CFEOM1 Mutations Attenuate KIF21A Autoinhibition and Cause
1130 Oculomotor Axon Stalling. *Neuron*, 82(2), pp.334–349.
- 1131 Cimini, D., Cameron, L.A. and Salmon, E.D., 2004. Anaphase spindle mechanics prevent mis-
1132 segregation of merotelically oriented chromosomes. *Current Biology*, 14(23), pp.2149–
1133 2155.
- 1134 Civelekoglu-Scholey, G. et al., 2013. Dynamic bonds and polar ejection force distribution
1135 explain kinetochore oscillations in PtK1 cells. *The Journal of Cell Biology*, 201(4), pp.577–
1136 593.
- 1137 Cousin, M.A. et al., 2019. RINT1 Bi-allelic Variations Cause Infantile-Onset Recurrent Acute
1138 Liver Failure and Skeletal Abnormalities. *American journal of human genetics*, 105(1),
1139 pp.108–121.
- 1140 Coy, D.L. et al., 1999. Kinesin's tail domain is an inhibitory regulator of the motor domain.
1141 *Nature cell biology*, 1(5), pp.288–292.
- 1142 Dodds, G.S., 1930. Row formation and other types of arrangement of cartilage cells in
1143 endochondral ossification. *The Anatomical Record*, 46(4), pp.385–399.
- 1144 Espeut, J. et al., 2008. Phosphorylation Relieves Autoinhibition of the Kinetochores Motor Cenp-
1145 E. *Molecular cell*, 29(5), pp.637–643.
- 1146 Friedman, D.S. and Vale, R.D., 1999. Single-molecule analysis of kinesin motility reveals
1147 regulation by the cargo-binding tail domain. *Nature cell biology*, 1(5), pp.293–297.
- 1148 Fu, C. et al., 2009. Phospho-Regulated Interaction between Kinesin-6 Klp9p and Microtubule
1149 Bundler Ase1p Promotes Spindle Elongation. *Developmental Cell*, 17(2), pp.257–267.
- 1150 Funabiki, H. and Murray, A.W., 2000. The *Xenopus* chromokinesin Xkid is essential for
1151 metaphase chromosome alignment and must be degraded to allow anaphase chromosome
1152 movement. *Cell*, 102(4), pp.411–424.
- 1153 Gan, H. et al., 2019. KIF5B modulates central spindle organization in late-stage cytokinesis in
1154 chondrocytes. *Cell and Bioscience*, pp.1–16.
- 1155 Germani, A. et al., 2000. SIAH-1 interacts with alpha-tubulin and degrades the kinesin Kid by
1156 the proteasome pathway during mitosis. *Oncogene*, 19(52), pp.5997–6006.
- 1157 Gillingham, A.K. and Munro, S., 2000. The PACT domain, a conserved centrosomal targeting
1158 motif in the coiled-coil proteins AKAP450 and pericentrin. *EMBO reports*, 1(6), pp.524–529.
- 1159 Haila, S. et al., 2001. SLC26A2 (diastrophic dysplasia sulfate transporter) is expressed in
1160 developing and mature cartilage but also in other tissues and cell types. *The journal of
1161 histochemistry and cytochemistry : official journal of the Histochemistry Society*, 49(8),
1162 pp.973–982.

- 1163 Hammond, J.W. et al., 2010. Autoinhibition of the kinesin-2 motor KIF17 via dual intramolecular
1164 mechanisms. *The Journal of Cell Biology*, 189(6), pp.1013–1025.
- 1165 Hammond, J.W. et al., 2009. Mammalian Kinesin-3 Motors Are Dimeric In Vivo and Move by
1166 Processive Motility upon Release of Autoinhibition M. Schliwa, ed. *PLOS Biology*, 7(3),
1167 pp.e1000072–14.
- 1168 Hatch, E.M. et al., 2013. Catastrophic Nuclear Envelope Collapse in Cancer Cell Micronuclei.
1169 *Cell*, 154(1), pp.47–60.
- 1170 Hershko, A., 1999. Mechanisms and regulation of the degradation of cyclin B. *Philosophical*
1171 *transactions of the Royal Society of London. Series B, Biological sciences*, 354(1389),
1172 pp.1571–5– discussion 1575–6.
- 1173 Iemura, K. and Tanaka, K., 2015. Chromokinesin Kid and kinetochore kinesin CENP-E
1174 differentially support chromosome congression without end-on attachment to microtubules.
1175 *Nature communications*, 6, pp.1–11.
- 1176 Imanishi, M. et al., 2006. Autoinhibition regulates the motility of the *C. elegans* intraflagellar
1177 transport motor OSM-3. *The Journal of Cell Biology*, 174(7), pp.931–937.
- 1178 Ioannidis, N.M. et al., 2016. REVEL: An Ensemble Method for Predicting the Pathogenicity of
1179 Rare Missense Variants. *The American Journal of Human Genetics*, 99(4), pp.877–885.
- 1180 Khandelia, P., Yap, K. and Makeyev, E.V., 2011. Streamlined platform for short hairpin RNA
1181 interference and transgenesis in cultured mammalian cells. *Proceedings of the National*
1182 *Academy of Sciences of the United States of America*, 108(31), pp.12799–12804.
- 1183 Lefeber, D.J., Morava, E. and Jaeken, J., 2011. How to find and diagnose a CDG due to
1184 defective N-glycosylation. *Journal of inherited metabolic disease*, 34(4), pp.849–852.
- 1185 Levesque, A.A. and Compton, D.A., 2001. The chromokinesin Kid is necessary for chromosome
1186 arm orientation and oscillation, but not congression, on mitotic spindles. *The Journal of Cell*
1187 *Biology*, 154(6), pp.1135–1146.
- 1188 Levesque, A.A. et al., 2003. A functional relationship between NuMA and kid is involved in both
1189 spindle organization and chromosome alignment in vertebrate cells. *Molecular biology of*
1190 *the cell*, 14(9), pp.3541–3552.
- 1191 Liu, D. et al., 2010. Regulated targeting of protein phosphatase 1 to the outer kinetochore by
1192 KNL1 opposes Aurora B kinase. *The Journal of Cell Biology*, 188(6), pp.809–820.
- 1193 Liu, Y. et al., 2018. Genomic, Proteomic and Phenotypic Heterogeneity in HeLa Cells across
1194 Laboratories: Implications for Reproducibility of Research Results. *bioRxiv*, p.307421.
- 1195 Marquis, C. et al., 2021. Chromosomally unstable tumor cells specifically require KIF18A for
1196 proliferation. *Nature communications*, pp.1–14.
- 1197 Marshall, W.F. et al., 2001. Chromosome elasticity and mitotic polar ejection force measured in
1198 living *Drosophila* embryos by four-dimensional microscopy-based motion analysis. *Current*
1199 *Biology*, 11(8), pp.569–578.

- 1200 Min, B.-J. et al., 2011. Whole-exome sequencing identifies mutations of KIF22 in
1201 spondyloepimetaphyseal dysplasia with joint laxity, leptodactylic type. *American journal of*
1202 *human genetics*, 89(6), pp.760–766.
- 1203 Morgan, D.O., 1995. Principles of CDK regulation. *Nature*, 374(6518), pp.131–134.
- 1204 Nislow, C. et al., 1992. A plus-end-directed motor enzyme that moves antiparallel microtubules
1205 in vitro localizes to the interzone of mitotic spindles. *Nature*, 359(6395), pp.543–547.
- 1206 Ohsugi, M. et al., 2003. Cdc2-mediated phosphorylation of Kid controls its distribution to spindle
1207 and chromosomes. *The EMBO journal*, 22(9), pp.2091–2103.
- 1208 Ohsugi, M. et al., 2008. Kid-Mediated Chromosome Compaction Ensures Proper Nuclear
1209 Envelope Formation. *Cell*, 132(5), pp.771–782.
- 1210 Quang, D., Chen, Y. and Xie, X., 2015. DANN: a deep learning approach for annotating the
1211 pathogenicity of genetic variants. *Bioinformatics (Oxford, England)*, 31(5), pp.761–763.
- 1212 Ren, J. et al., 2018. Coiled-coil 1-mediated fastening of the neck and motor domains for kinesin-
1213 3 autoinhibition. *Proceedings of the National Academy of Sciences of the United States of*
1214 *America*, 115(51), pp.E11933–E11942.
- 1215 Rentzsch, P. et al., 2018. CADD: predicting the deleteriousness of variants throughout the
1216 human genome. pp.1–9.
- 1217 Rieder, C.L. and Salmon, E.D., 1994. Motile kinetochores and polar ejection forces dictate
1218 chromosome position on the vertebrate mitotic spindle. *The Journal of Cell Biology*, 124(3),
1219 pp.223–233.
- 1220 Rieder, C.L. et al., 1986. Oscillatory movements of monooriented chromosomes and their
1221 position relative to the spindle pole result from the ejection properties of the aster and half-
1222 spindle. *The Journal of Cell Biology*, 103(2), pp.581–591.
- 1223 Ris, H., 1949. The anaphase movement of chromosomes in the spermatocytes of the
1224 grasshopper. *The Biological bulletin*, 96(1), pp.90–106.
- 1225 Rossi, A. and Superti-Furga, A., 2001. Mutations in the diastrophic dysplasia sulfate transporter
1226 (DTDST) gene (SLC26A2): 22 novel mutations, mutation review, associated skeletal
1227 phenotypes, and diagnostic relevance. *Human Mutation*, 17(3), pp.159–171.
- 1228 Samwer, M. et al., 2017. DNA Cross-Bridging Shapes a Single Nucleus from a Set of Mitotic
1229 Chromosomes. *Cell*, 170(5), pp.956–972.e23.
- 1230 Sawin, K.E. et al., 1992. Mitotic spindle organization by a plus-end-directed microtubule motor.
1231 *Nature*, 359(6395), pp.540–543.
- 1232 Schindelin, J. et al., 2012. Fiji: an open-source platform for biological-image analysis. *Nature*
1233 *Methods*, 9(7), pp.676–682.
- 1234 Schneider, C.A., Rasband, W.S. and Eliceiri, K.W., 2012. NIH Image to ImageJ: 25 years of
1235 image analysis. *Nature Methods*, pp.1–5.

- 1236 Schwarz, J.M. et al., 2010. MutationTaster evaluates disease-causing potential of sequence
1237 alterations. *Nature Publishing Group*, pp.1–2.
- 1238 Serra-Marques, A. et al., 2020. The mitotic protein NuMA plays a spindle-independent role in
1239 nuclear formation and mechanics. *The Journal of Cell Biology*, 219(12), pp.348–23.
- 1240 Shiroguchi, K. et al., 2003. The Second Microtubule-binding Site of Monomeric Kid Enhances
1241 the Microtubule Affinity. *The Journal of biological chemistry*, 278(25), pp.22460–22465.
- 1242 Soeda, S., Yamada-Nomoto, K. and Ohsugi, M., 2016. The microtubule-binding and coiled-coil
1243 domains of Kid are required to turn off the polar ejection force at anaphase. *Journal of cell
1244 science*, 129(19), pp.3609–3619.
- 1245 Straight, A.F., Sedat, J.W. and Murray, A.W., 1998. Time-lapse microscopy reveals unique roles
1246 for kinesins during anaphase in budding yeast. *The Journal of Cell Biology*, 143(3), pp.687–
1247 694.
- 1248 Stumpff, J. et al., 2012. Kif18A and Chromokinesins Confine Centromere Movements via
1249 Microtubule Growth Suppression and Spatial Control of Kinetochore Tension.
1250 *Developmental Cell*, 22(5), pp.1017–1029.
- 1251 Stumpff, J. et al., 2008. The Kinesin-8 Motor Kif18A Suppresses Kinetochore Movements to
1252 Control Mitotic Chromosome Alignment. *Developmental Cell*, 14(2), pp.252–262.
- 1253 Sturgill, E.G. et al., 2016. Kinesin-5 inhibitor resistance is driven by kinesin-12. *The Journal of
1254 Cell Biology*, 213(2), pp.213–227.
- 1255 Su, K.-C. et al., 2016. A Regulatory Switch Alters Chromosome Motions at the Metaphase-to-
1256 Anaphase Transition. *Cell reports*, 17(7), pp.1728–1738.
- 1257 Takagi, J. et al., 2013. Chromosome position at the spindle equator is regulated by
1258 chromokinesin and a bipolar microtubule array. *Scientific Reports*, 3, pp.746–7.
- 1259 Tanenbaum, M.E. et al., 2009. Kif15 Cooperates with Eg5 to Promote Bipolar Spindle
1260 Assembly. *Current Biology*, 19(20), pp.1703–1711.
- 1261 Tokai, N. et al., 1996. Kid, a novel kinesin-like DNA binding protein, is localized to
1262 chromosomes and the mitotic spindle. *The EMBO journal*, 15(3), pp.457–467.
- 1263 Tokai-Nishizumi, N. et al., 2005. The chromokinesin kid is required for maintenance of proper
1264 metaphase spindle size. *Molecular biology of the cell*, 16(11), pp.5455–5463.
- 1265 Tüysüz, B. et al., 2014. Spondyloepimetaphyseal dysplasia with joint laxity, leptodactylic type:
1266 longitudinal observation of radiographic findings in a child heterozygous for a KIF22
1267 mutation. *Pediatric Radiology*, 45(5), pp.771–776.
- 1268 Uhlen, M. et al., 2015. Tissue-based map of the human proteome. *Science (New York, N.Y.)*,
1269 347(6220), pp.1260419–1260419.
- 1270 van der Vaart, B. et al., 2013. CFEOM1-Associated Kinesin KIF21A Is a Cortical Microtubule
1271 Growth Inhibitor. *Developmental Cell*, 27(2), pp.145–160.

- 1272 van Heesbeen, R.G.H.P., Tanenbaum, M.E. and Medema, R.H., 2014. Balanced Activity of
1273 Three Mitotic Motors Is Required for Bipolar Spindle Assembly and Chromosome
1274 Segregation. *Cell reports*, 8(4), pp.948–956.
- 1275 Vaser, R. et al., 2015. SIFT missense predictions for genomes. *Nature Protocols*, 11(1), pp.1–9.
- 1276 Verhey, K.J. and Hammond, J.W., 2009. Cytoskeletal motors: Traffic control: regulation of
1277 kinesin motors. pp.1–13.
- 1278 Verhey, K.J. et al., 1998. Light chain-dependent regulation of Kinesin's interaction with
1279 microtubules. *The Journal of Cell Biology*, 143(4), pp.1053–1066.
- 1280 Vukušić, K. et al., 2021. Microtubule-sliding modules based on kinesins EG5 and PRC1-
1281 dependent KIF4A drive human spindle elongation. *Developmental Cell*, pp.1–42.
- 1282 Vukušić, K., Buđa, R. and Tolić, I.M., 2019. Force-generating mechanisms of anaphase in
1283 human cells. *Journal of cell science*, 132(18), pp.jcs231985–11.
- 1284 Wandke, C. et al., 2012. Human chromokinesins promote chromosome congression and spindle
1285 microtubule dynamics during mitosis. *The Journal of Cell Biology*, 198(5), pp.847–863.
- 1286 Wolf, F. et al., 2006. Dose-dependent effects of stable cyclin B1 on progression through mitosis
1287 in human cells. *The EMBO journal*, 25(12), pp.2802–2813.
- 1288 Yajima, J. et al., 2003. The human chromokinesin Kid is a plus end-directed microtubule-based
1289 motor. *The EMBO journal*, 22(5), pp.1067–1074.
- 1290 Yount, A.L., Zong, H. and Walczak, C.E., 2015. Regulatory mechanisms that control mitotic
1291 kinesins. *Experimental Cell Research*, 334(1), pp.70–77.
- 1292 Zhang, P. et al., 1990. A kinesin-like protein required for distributive chromosome segregation in
1293 *Drosophila*. *Cell*, 62(6), pp.1053–1062.